# Determination of invariant mass end-points in the mSUGRA coannihilation region

**by**

**Konstantinos A. Kastanas**


**Master Degree Thesis in Experimental Particle Physics**
**Department of Physics and Technology**
**University of Bergen**
**Norway**

**July 25, 2008**

# Acknowledgements

First of all I would like to thank all the great people in the particle physics group in Bergen, thank you all for making this such a great place to be and for all your help in writing this thesis. Hilde Skjerdal, Maren Ugland and Therese Sjursen deserve special thanks for all the good times and their support. Therese Sjursen I'd further like to thank for her collaboration in this analysis, for the help, discussions and for making this whole project even more fun.

Oystein Djuvsland I'd like to thank for fun times, the various side-projects and general silliness. And of course Kelly Kanaki for all the laughs and some fantastic gastronomic support!

To Anna Lipniacka, my supervisor, thank you for your encouragement, great guidance for this thesis and all the opportunities you have given me. Thomas Burgess I would also like to thank for reading through the thesis and many helpful suggestions.

Finally to my mother, family and friends, both in Iceland and in Greece, my greatest gratitude for your friendship, support and for always being there, even when you are all so far away.

Alex Kastanas

# Contents

# List of Figures

# Preface

The topic of this thesis is the study of supersymmetry (SUSY) in the ATLAS detector. A SUSY decay chain in the mSUGRA scenario involving two tau leptons has been studied. The end-points of the invariant mass distributions of the visible decay products of the chain can yield information on the unknown sparticle masses. Four such end-points have been analysed. Furthermore, a new version of the tau reconstruction algorithm was tried to see if any improvement can be made compared to the old algorithm.

Chapter one provides an introduction to the Standard Model, the physical description of modern particle physics, whereas chapter two contains a description of Supersymmetry, a possible extension of the Standard Model studied in this thesis. The studies have been carried out for the ATLAS experiment, described in chapter three as well as the LHC accelerator. Chapter four explains some basics of the reconstruction of tau particles, jets and missing energy which are the objects used in the study and the performance of the new version of tau reconstruction is evaluated. Chapter five contains the main subject of the thesis, the analysis of the end-points of the invariant mass distributions in the coannihilation region.

# Chapter 1

# Standard Model

The *Standard Model* (SM) of Particle Physics is the effective theory describing all high energy physics phenomena known today. The mathematical theory describing the physics therein is called *Quantum Field Theory* (QFT). In a quantum field theory particles are described by quantized fields and their interactions are mediated by gauge fields. In this chapter the basic formalism behind the theory is introduced, as well as the basic features of the model. This chapter is based upon the treatment given in [1].

## 1.1 An overview

The particle content of the SM can be divided into two distinct categories, the *fermions* and the *bosons*, having half-integer and integer spin respectively. The fermions make up the matter particles of the SM. The bosons of spin one mediate the interactions of the SM and the spin zero Higgs boson gives mass to all massive particles. An overview of the particle content can be found in table 1.1. The properties of these particles as defined by their quantum numbers determine what interactions are observed between them in nature.

### 1.1.1 Electromagnetic interactions

In the SM electromagnetic interactions are mediated by the photon, the quantum of the electromagnetic field. It is a massless, spin one particle. Since it is massless, the electrostatic field leads to the Coulomb force with an infinite range. The theory describing this interaction is *Quantum Electro Dynamics* (QED), see section 1.4.1.

### 1.1.2 Weak interactions

The weak force is best known from $\beta$-decay. It is weaker than the other two forces due to its mediating bosons', the $Z^0$ and the $W^{\pm}$, large mass. It couples to all the SM fermions but with unequal coupling to left- and right-handed parts, see section 1.4.2.

### 1.1.3 Strong interaction

The strong force is carried by the gluons which, like the photon, are massless. The strong force couples to the colour charge, which is carried by the quarks *and the gluons themselves*. In particular, gluons carry both a colour and an anticolour charge.

There are two important features of the strong force, namely confinement and asymptotic freedom. Confinement states that no free colour charge can be observed, all free states are colour neutral. This leads the the existence of *hadrons*, bound states of quarks forming colour neutral objects. Asymptotic freedom means that the quarks inside hadrons do not feel the strong force, they behave as free particles.

### 1.1.4 Fermions

The fermion sector can be dissected in two ways. By looking at similarities between fermions, three *generations* can be identified. These are three identical copies of the same structure with only the mass of the fermions being different. Looking at the characteristics of fermions on the other hand, two categories are observed, the *leptons* and the *quarks*. The leptons include the charged leptons, such as the electron, and the electrically neutral neutrinos. Both types interact weakly as well. Of the charged leptons only the electron is stable, whereas the muon and the tau are unstable, both decaying via the weak force.

All the fermions have a distinct antiparticle as well, with all quantum charges opposite, but all other properties unchanged. Bosons on the other hand are their own antiparticles. The existence of these states is necessary if the theory is to be consistent with relativity.

As with the leptons, the quarks interact via the electromagnetic and weak force but are set apart by the fact that they also interact strongly. Each family has two quarks, one with charge $2/3e$ (up-type) and one with $-1/3e$(down-type), where $e$ is the elementary charge. These fractional charges are never observed, however, as the quarks are only found in bound states of three (anti)quarks, the *baryons*, or a quark-antiquark pair, the *mesons*. Quarks also carry color charge, the charge associated with strong interactions. The colour charge carried by the quarks is either blue, red or green, with antiquarks carrying anticolour.

## 1.2 Fermionic fields

The first step in constructing the Standard Model is to introduce the matter fields it describes. These are the spin 1/2 fields (*fermions*) such as electrons and quarks. First they are given as free fields and then, by arguments of symmetry, their interactions can be introduced.

Table 1.1: An overview of the particle content of the SM.

| Fermions | | | | Bosons | | |
|---|---|---|---|---|---|---|
| **Generation** | **I** | **II** | **III** | **Force** | **Mediator** | **Mass** |
| **Quarks** | u | c | t | **Strong force** | g | 0 |
| | d | s | b | | | |
| **Leptons** | e | $\mu$ | $\tau$ | **Electromagnetic** | $\gamma$ | 0 |
| | $\nu_e$ | $\nu_\mu$ | $\nu_\tau$ | **Weak force** | $W^{\pm}$, $Z^0$ | 80, 91 GeV |
| | | | | **Higgs boson** | $H^0$ | $> 114.4$ GeV |

The first step in this was done by Dirac in 1928 who, using the following equation, described the dynamics of relativistic massive fermions. Dirac's equation can be written as follows

$$i\gamma^\mu \frac{\partial \psi(x)}{\partial x^\mu} - m\psi(x) = 0 \tag{1.1}$$

The $\gamma^\mu$'s are the $4 \times 4$ Dirac matrices, satisfying the anticommutation relations

$$[\gamma^\mu, \gamma^\nu] = 2g^{\mu\nu} \tag{1.2}$$

The wavefunction $\psi(x)$ is a four-component spinor wavefuntion. Comparing this to the Schröedinger equation, it is clear that incorporating spin and the Einstein energy momentum relation has resulted in quadrupling the degrees of freedom. For spin 1/2 particles an extra two degrees of freedom are expected due to two possible spin states. The further two come from the existence of anti-particles.

The Dirac equation is consistent with the following *Lagrangian*

$$\mathcal{L} = \bar{\psi}(x) \left[ i\gamma^\mu \frac{\partial}{\partial x^\mu} - m \right] \psi(x) \tag{1.3}$$

The terms in this Lagrangian can be seen as the kinetic and the mass term for the field. In order to move to a particle interpretation, a procedure called second quantization is employed; the details, however, are not very illuminating so they will be spared in this context.

Interactions are introduced to the system through terms that contain different fields. However, it is far from clear what form these terms should have in principle. Symmetry can be employed as the guiding principle behind such additions and leads to experimentally confirmed results in the case of EM interaction.

Table 1.2: Properties of groups

| | |
|---|---|
| **Associativity** | $a \times (b \times c) = (a \times b) \times c$ for all $a, b, c \in G$ |
| **Identity element** | There exists an element $e$ such that $e \times a = a \times e = a$ |
| **Inverse** | For every $a \in G$ exists an element $a^{-1}$ where $a \times a^{-1} = e$ |

## 1.3 Symmetry groups

In the SM we are interested in the three so-called gauge symmetries which are the guiding principle behind interaction terms in the Lagrangian. To get a better understanding and a mathematical foothold the language of group theory is used.

### 1.3.1 Basics of group theory

A group, $G$, is a set of elements and a bilinear operation, noted here by $\times$. The properties of groups are summarized in table 1.2.

Furthermore, a group may be commutative or *Abelian*, i.e. $a \times b = b \times a$. This distinction will prove to be very important in what follows.

It is useful to find generators for the groups, denoted here by $\tau_i$. The importance of these lies in that any element in the group can be written using the generators and the group operation.

But in general a group is an abstract entity, the elements are merely algebraic symbols with certain relationships defined. In order to make groups useful a representation is needed. This means finding a set of numbers or matrices that have the same behaviour as the group elements.

### 1.3.2 Symmetry groups

Using the tools of group theory, the symmetries of physics can be systematically treated, but what do such symmetries tell us about the world? Quite a lot, as is strikingly shown in Emmy Noether's theorem [2]. It states that for any symmetry in physics there exists an associated conserved quantity and/or current and vice-versa. Furthermore, knowing the transformation under which the Lagrangian is invariant the conserved quantities can be extracted mathematically. Not only does this simplify the physics, but in the case of the SM it also defines the charges and currents involved in the different interactions to be determined solely from the corresponding symmetry.

## 1.4 Symmetries of the SM

Three gauge groups are the most important groups in the SM, each one defining one of the three SM interactions.

### 1.4.1 Electromagnetism, $U(1)$

The U(1) group is the group of all complex numbers of modulus one and the corresponding transformation can be written as

$$\psi(x) \rightarrow \psi'(x) = \psi(x)e^{iqf(x)} \tag{1.4}$$

The transformations furnished by this group are known from classical electromagnetism. There they appear in the form of the arbitrary gauge of the scalar and vector fields. Here, these transformations work on both the vector field and the interacting fermions.

If the theory is to be invariant under this gauge group the Lagrangian should be left unmodified by this transformation[1]. As is plainly seen the kinetic term will be altered, due to the derivative being there. The solution to this problem is to modify the derivative to contain a term that counteracts this extra term. The resulting derivative is referred to as a covariant derivative, since the derivative itself now changes under the transformation. The term added is

$$\partial^\mu \rightarrow D^\mu = \partial^\mu + iqA^\mu(x)\,. \tag{1.5}$$

This substitution is referred to as the minimal substitution, where $A^\mu(x)$ describes the photon field. Now, looking at the terms in the Lagrangian, this adds a third one, a term of the form

$$\mathcal{L}_{int} = iq\bar{\psi}(x)A^\mu(x)\psi(x)\,. \tag{1.6}$$

This term is interpreted as an interaction term, between two fermions ($\psi(x)$ and $\bar{\psi}(x)$) and a photon ($A^\mu(x)$). The photon field, under the U(1) group, transforms as

$$A^\mu(x) \rightarrow A'^\mu(x) = A^\mu(x) + \partial^\mu\alpha(x)\,, \tag{1.7}$$

leaving the physically measurable fields, **E** and **B**, unchanged.

The Lagrangian is invariant under this set of transformations, collectively referred to as the U(1) gauge transformations. Furthermore, as Noether's theorem implies there is an associated conserved current

$$s^\alpha(x) = -e\bar{\psi}(x)\gamma^\alpha\psi(x) \tag{1.8}$$

1. Or modified up to a total derivative to be exact.

and $q$ can be identified as the charge of the interacting fermion, e.g. $q = -e$ in the case of the electron.

The important thing about this transformation is that the coupling term is introduced only by argument of symmetry. This is the blueprint on which all gauge theories are based, identify the symmetry group and then introduce the terms necessary to make the Lagrangian invariant under its transformations.

### 1.4.2 Electroweak theory, $SU(2) \times U(1)$

The weak force is perhaps the most striking force in the SM. It is associated with symmetry breaking, such as parity violation, having massive gauge bosons and as a result a very weak coupling. All these concepts are covered within the electroweak theory, the theory that includes electromagnetism and the weak interaction in a unified framework.

First, one needs to look at some of the properties of the weak interaction. Experimentally it can be seen that the coupling is different between left- and right-handed fermions. For any given fermion in a state $\psi(x)$ the states with definite chirality can be projected out with the operator $P_{L/R}$ defined as

$$\psi_{L/R}(x) = P_{L/R}\psi(x) = \frac{1}{\sqrt{2}}\left(1 \mp \gamma_5\right) . \tag{1.9}$$

The theory is built up from the $SU_L(2) \times U_Y(1)$ group, the $L/R$ subscript put there to indicate that the group couples to chiral fields. Of the two groups, $U(1)_Y$ is already familiar from the previous section. The $SU(2)_L$ group is the group of all special, unitary $2 \times 2$ matrices. It is non-Abelian and can be represented by $2 \times 2$ matrices. The transformations furnished by the SU(2) group act upon doublets, meaning the wavefunctions are in the form of a two-component vectors. The generators are given as $t^\alpha = \sigma^\alpha/2$ where $\sigma^\alpha$ are the familiar Pauli matrices

$$\sigma^1 = \begin{pmatrix} 0 & 1 \\ 1 & 0 \end{pmatrix}, \quad \sigma^2 = \begin{pmatrix} 0 & -i \\ i & 0 \end{pmatrix}, \quad \sigma^3 = \begin{pmatrix} 1 & 0 \\ 0 & -1 \end{pmatrix}.$$

The doublets chosen are the left-handed leptons and quarks within each family $\Psi_L(x) = \begin{pmatrix} \psi_L^{\nu_l}(x) \\ \psi_L^{l}(x) \end{pmatrix}$ for the leptons and $\Psi_L(x) = \begin{pmatrix} \psi_L^{u}(x) \\ \psi_L^{d}(x) \end{pmatrix}$ for the quarks. The SU(2) transformation now acts upon these states

$$\Psi(x) \rightarrow \Psi'(x) = e^{-i\alpha^\alpha(x)t^\alpha}\Psi(x) . \tag{1.10}$$

and thereby effectively mixes the charged and neutral lepton states and the up and down type quarks in each family.

The right-handed states are singlets under the SU(2) group and thus are invariant under the transformation. In this formalism the free Lagrangian density for

the fermions can be written as

$$\mathcal{L} = i\left[\bar{\Psi}_l^L(x)\,\partial\!\!\!/\Psi_l^L(x) + \bar{\psi}_l^R(x)\,\partial\!\!\!/\psi_l^R(x) + \bar{\psi}_{\nu_l}^R\,\partial\!\!\!/\psi_{\nu_l}^R(x)\right], \tag{1.11}$$

where the slash notation is used, $\partial\!\!\!/ = \gamma^\mu\partial_\mu$.

The three currents under this transformation are

$$J_\mu^\alpha = \bar{\Psi}(x)\gamma_\mu t^\alpha \Psi(x)\,. \tag{1.12}$$

Further, the weak hypercharge current, associated with the $U(1)_Y$ is expressed as

$$J_Y^\alpha = J_{QED}^\alpha(x) - J_3^\alpha(x) \tag{1.13}$$

where $J_{QED}$ is the conserved current of QED and the associated charge

$$Y = Q - I_3\,. \tag{1.14}$$

The charge $Y$ is called the *hypercharge* and $I_3$ is the third component of *weak isospin*. This naming convention is chosen due to the close resemblance to nuclear isospin. This is how the $U(1)_{QED}$ gauge group of QED can be replaced with the $SU(2)_L \times U(1)_Y$ of electroweak theory.

Finally, the full Lagrangian of the theory is

$$\begin{aligned}\mathcal{L} = \mathcal{L}_0 + \mathcal{L}_I \;=\; & \mathcal{L}_0 - s^\mu(x)A_\mu(x) \\ & -\frac{g}{2\sqrt{2}}\left[J^{\dagger\mu}(x)W_\mu(x) + J^\mu(x)W_\mu^\dagger(x)\right] \\ & -\frac{g}{cos\theta_W}\left[J_3^\mu(x) - sin^2\theta_W\, s^\mu(x)/e\right]\,.\end{aligned} \tag{1.15}$$

It is not possible however to write a gauge-invariant mass term for vector fields. Experimentally, it is known that the $W^\pm$ and $Z^0$ are both massive, 80 and 91 GeV respectively [3]. Hence, the $SU_L(2) \times U_Y(1)$ symmetry of electroweak theory, despite its successful predictions cannot be exact and must be broken in some way.

### 1.4.3 Symmetry breaking

There are two conditions for an exact symmetry in physics; it must be a symmetry of both the Lagrangian and the lowest energy state of the system. This is indeed the case for all the exact symmetries seen so far. But if the latter condition is not satisfied the symmetry is hidden. This is referred to as spontaneous symmetry breaking.

The solution to the problem of *electroweak symmetry breaking* (EWSB), proposed in its SM implementation by Higgs in 1966 [4] is to use a scalar field with

a non-zero *Vacuum Expectation Value* (VEV) in order to break the $SU_L(2) \times U_Y(1)$ symmetry, leaving only $U_{QED}(1)$, the symmetry of QED. With this mechanism the theory can still have the underlying symmetry, but the symmetry is hidden because the vacuum does not respect it, this is referred to as spontaneous breaking.

In order to construct such a mechanism, one first introduces a scalar doublet complex field, $\phi$, with Lagrangian density

$$\mathcal{L} = \partial^\mu \phi^\dagger \partial_\mu \phi - \mu\, \phi^\dagger \phi - \lambda^2 \left(\phi^\dagger \phi\right)^2 . \tag{1.16}$$

where $\mu$ is the Higgs mass parameter and $\lambda$ is the Higgs self-coupling parameter.

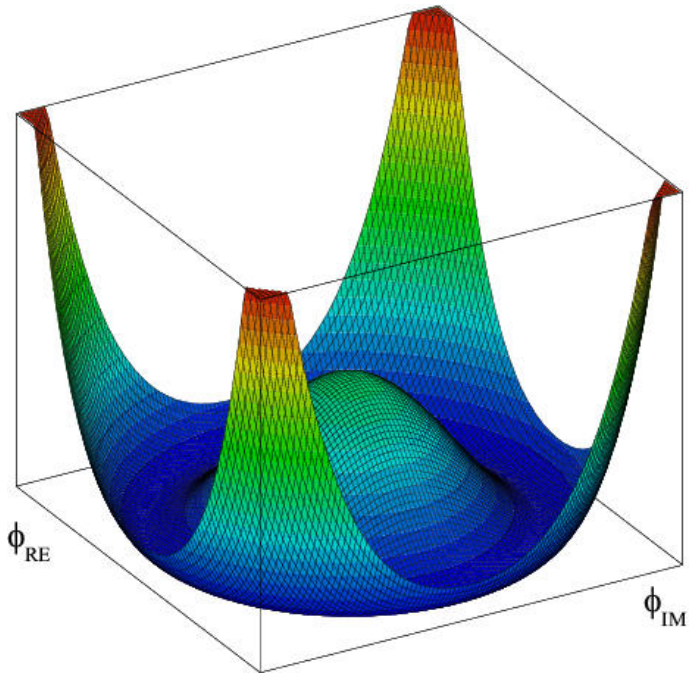


Figure 1.1: The form of the Higgs potential, showing the Mexican hat shape.

If the constants $\mu$ and $\lambda$ are chosen appropriately the potential takes the form of a Mexican hat, with a continuous infinity of degenerate vacua, as well as an unstable vacuum for $\phi(x) = 0$. The form of the potential is shown in figure 1.1. Since this middle vacuum is unstable and therefore not suitable for perturbation expansion, one of the degenerate vacua has to be chosen. It is this choice of a vacuum that breaks the symmetry, while the Lagrangian is symmetric the ground state is not.

Promoting the derivatives in 1.16 to $SU(2) \times U(1)$ covariant derivatives, using

the substitution

$$\partial^\mu \phi \rightarrow D^\mu \phi = \partial^\mu \phi - igA^{a\,\mu}\frac{\sigma^a}{2}\phi - i\frac{g'}{2}B_\mu \phi\,, \tag{1.17}$$

we obtain the couplings of the Higgs doublet to the gauge fields.

Moving to a specific vacuum state, e.g.

$$\langle \Phi \rangle = \frac{v}{\sqrt{2}}\begin{pmatrix}0\\1\end{pmatrix} = \sqrt{-\frac{\mu^2}{2\lambda}}\begin{pmatrix}0\\1\end{pmatrix}, \tag{1.18}$$

we can see that the mass eigenstates of the system and their eigenvalues become

$$W^\pm_\mu = \frac{A^1_\mu \mp i A^2_\mu}{\sqrt{2}}, \quad M_W = \frac{gv}{2} \tag{1.19}$$

$$Z^0_\mu = \frac{gA^3_\mu - g'B_\mu}{\sqrt{g^2+g'^2}}, \quad M_Z = \frac{\sqrt{g^2+g'^2}}{2}v \tag{1.20}$$

$$A_\mu = \frac{g'A^3_\mu + gB_\mu}{\sqrt{g^2+g'^2}}, \quad M_A = 0 \tag{1.21}$$

where

$$g\sin\theta_W = g'\cos\theta_W = e \tag{1.22}$$

and $\theta_W$ is the weak mixing angle, or Weinberg angle, describing the amount of mixing between the weak and the electromagnetic sectors. It can be measured by noting that

$$\cos\theta_W = \frac{M_W}{M_Z} \tag{1.23}$$

It is experimentally found to be $\sin^2(\theta_W) = 0.2326$ [3].

Using the Higgs mechanism, the fields $W^\pm$ and $Z^0$ have acquired mass and the photon field $A$ has been recovered and remains massless. In other words the choice in eq. (1.18) gives the familiar $U(1)_{QED}$ after symmetry breaking, as is required and hides the underlying $SU(2)_L \times U(1)_Y$. This further results in one massive spin zero boson entering the theory, the Higgs boson, with mass:

$$m_{H^0} = \sqrt{2\lambda v^2} \tag{1.24}$$

### 1.4.4 Overview of internal symmetries

In the following table the properties of the SM particles under the groups are reviewed.

Table 1.3: An overview of the quantum numbers of the different fields in the SM.

| | $SU(3)_C$ | $SU(2)_L$ | $U(1)_Y$ |
|---|---|---|---|
| $L = \begin{pmatrix} \nu_L \\ e_L \end{pmatrix}$ | **1** | **2** | -1 |
| $e_R$ | **1** | **1** | -2 |
| $Q = \begin{pmatrix} u_L \\ d_L \end{pmatrix}$ | **3** | **2** | $\frac{1}{3}$ |
| $u_R$ | **3** | **1** | $\frac{4}{3}$ |
| $d_R$ | **3** | **1** | $-\frac{2}{3}$ |

## 1.5 External symmetries

In addition to the above symmetries of the SM Lagrangian there are also the external, space-time, symmetries of special relativity. These make up the Poincaré group and the constituent symmetries are

- Space-time translations, $P_\mu$, associated with conservation of momentum and energy.
- Lorentz transformations(rotations and boosts), $M_{\mu\nu}$ are the symmetries of special relativity. Rotations are associated with conservation of angular momentum whereas boosts are the symmetry under change of reference system.

The algebra of these operators is

$$\begin{aligned} [P^\mu, P^{nu}] &= 0 && (1.25)\\ [M_{\mu\nu}, P_\rho] &= g_{\mu\rho}P_\nu - g + \nu\rho P_\mu && (1.26)\\ [M_{\mu\nu}, M_{\rho\sigma}] &= g_{\mu\rho}M_{\nu\sigma} - g_{\mu\sigma}M_{\nu\rho} && (1.27)\\ &\quad -g_{\nu\rho}M_{\mu\sigma} + g_{\nu\sigma}M_{\nu\rho}\,. \end{aligned}$$

## 1.6 Shortcomings of the SM

The Standard Model describes most, if not all, experimental phenomena in particle physics seen today but has a number of undesirable features.

**Hierarchy problem** The mass of the Higgs boson in the SM is constrained by the masses of SM particles, the top quark and W boson most importantly. But if one is to do a direct calculation of its mass the higher order corrections become large and a very precise cancellation of these is necessary to produce the expected mass. This is known as the hierarchy problem.

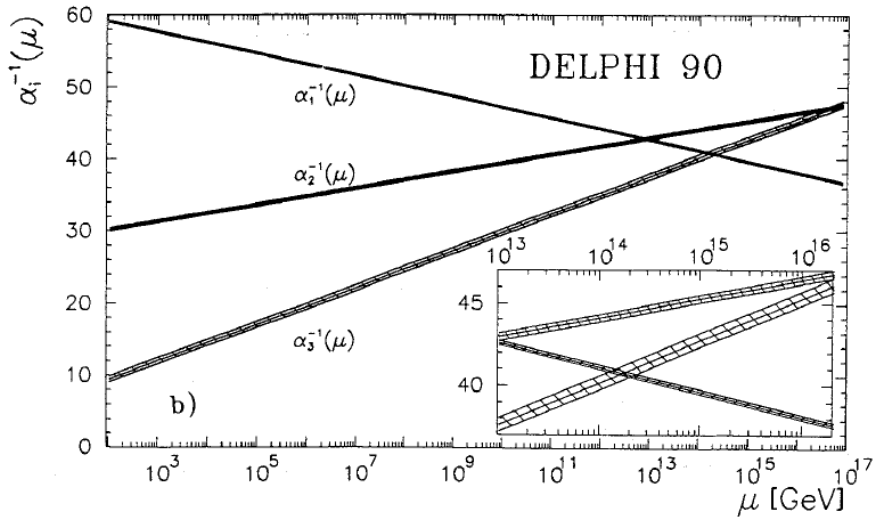


Figure 1.2: The coupling constants of the SM are energy dependent. Figure is taken from [5]

**Free parameters** The SM includes 20 free parameters, that are put in from experimental data.

**Grand Unification** The running couplings of the SM almost unify at a large scale, $M_{GUT}$, but not quite. Theories beyond the SM that alter the running of the coupling constants can produce unification [5]. See figure 2.1.

**No-go theorem** It has been shown that the symmetries of the SM cannot be unified with those of the Poinceré group. This is known as the no-go theorem [6].

**Dark Matter** The SM provides no candidate for *dark matter*, DM, which is required by experimental data from cosmology [7].

**Neutrino masses** are not presently included in the SM, though there are experimental evidence that at least *some of them* are non-zero

# Chapter 2

# Supersymmetry

As seen above the SM is a very good effective theory at the energies where it has been tested. However, much is left to be desired in terms of *explaining* why the structure of the theory is as it is. For this an extension is necessary and one such extension, *SUperSYmmetry* (SUSY) is explained below.

This chapter is not intended as a full introduction to SUSY. It will rather show some of its basic properties and then focus on the features that may be seen in the LHC.

## 2.1 Overview of SUSY

The basic idea of SUSY is that for each particle in the SM there exists a *superpartner*, or *sparticle*. These have the same properties as their SM partner with the exception of their spin, differing by one-half. Together the SM particle and the superpartner form a so-called supermultiplet. Three kinds of multiplets come into play, depending on the spin of the SM particle in them.

**Chiral multiplets** are formed by the fermions of the SM and their superpartners, which have spin zero. The naming convention is to use the same name as their SM partner and adding a "s-" prefix, i.e. electron → selectron.

**Gauge multiplets** are formed from the gauge bosons of the SM and their superpartners. The superpartners carry spin 1/2 and are named after their SM partner plus the suffix "-ino", i.e. photon → photino.

**Scalar multiplets** are constituted of bosons in the Higgs sector and their superpartners. Their superpartners have spin 1/2 as well and follow the same naming convention as the gauge multiplets.

The inclusion of these states helps solve some of the problems of the SM:

- The hierarchy problem is solved, since the contributions of SM particles and their superpartners to the Higgs mass corrections cancel. This cancellation is exact as long as particles and their superpartners have the same mass.

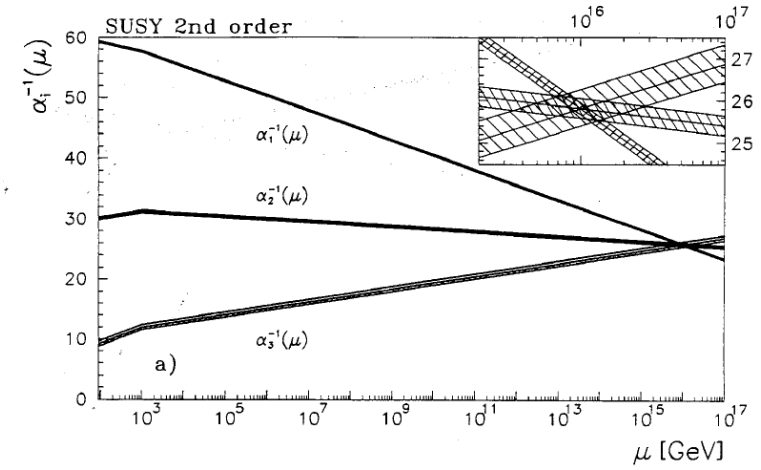


Figure 2.1: The extrapolation of the inverse coupling constants of the SM in light of SUSY. Figure is taken from [5].

- Dark matter candidates can be found within SUSY scenarios.
- The "no-go" theorem, see section 1.6, does not apply anymore. This is because it only covers normal Lie algebras and not the extended algebras of SUSY as is shown in [8].
- The running of the gauge couplings is altered when SUSY is included [5], making them unify at a large scale, see figure 2.1.

## 2.2 Basic theory

The operator $Q$ of SUSY acts on a fermion state $|f\rangle$, of spin $s$ to produce a boson state $|b\rangle$ of spin $s - 1/2$ so that

$$Q\,|f\rangle = |b\rangle\ . \tag{2.1}$$

The simplest supersymmetric algebra is obtained with only one supersymmetry charge $Q$, and can be written as

$$\{Q_r, \bar{Q}_s\} = 2\gamma^{\mu}_{rs}\, P_{\mu} \tag{2.2}$$
$$[Q_r, P^{\mu}] = 0 \tag{2.3}$$
$$[Q_r, M^{\mu\nu}] = i\sigma^{\mu\nu}_{rs}\, Q_s\,. \tag{2.4}$$

The above algebra uniquely defines SUSY. The SM extended by only one SUSY operator is commonly referred to as the *Minimal Supersymmetric Standard Model* (MSSM). Together equations (1.25)-(1.28) and (2.2)-(2.4) constitute a *super-Poincaré algebra*. An important consequence of the above equations is that

$$\left[Q_r, P_{\mu}P^{\mu}\right] = 0\,, \tag{2.5}$$

which implies that if two states, $|f\rangle$ and $|b\rangle$, are connected though the operator $Q$ their masses are equal. The two states are referred to as each other's *superpartners*. Since no such standard model superpartners have been observed, supersymmetry must be broken if it exists. To introduce different masses for the sparticles symmetry breaking terms are introduced in the Lagrangian, and with them a large number of free parameters enter the theory.

Finding a SUSY breaking mechanism is not completely open, since the form of the breaking term must still preserve the desirable features of SUSY, including a natural solution to the hierarchy problem. This somewhat constrains the number of possible breaking terms. However, the number of free parameters in broken SUSY remains greater than what is desirable for a good phenomenological model.

## 2.3 Superpartners

The theory introduces a new set of particles with one superpartner for each SM particle, the different superpartners are introduced below.

**Scalar sector** In the case of the fermions of the SM, the superpartner is a scalar particle. Because fermions have more degrees of freedom as they have spin, one scalar partner is introduced for each spin state. These are labelled $\tilde{f}_R$ and $\tilde{f}_L$ for the right- and left-handed states respectively.

**Higgs sector** In a SUSY theory it is not enough to have only one Higgs doublet. Two Higgs doublets are introduced, each responsible to giving masses to up- and down-type quarks respectively. This leads to five Higgs particles being present in the theory: $h$, $H$, $H^{\pm}$ and $A$. An interesting consequence of this change is that it naturally leads to *electroweak symmetry breaking* (EWSB) in a large area of the parameter space.

**Fermion sector** The fermion sector of the supersymmetric spectrum consists of the superpartners of the SM gauge bosons and the two Higgs doublets. After symmetry breaking the partners of the photon, the $Z^0$ and the two Higgs superpartners will mix to form four neutralino states, $\chi_i^0$. The partner of the $W^{\pm}$ and the charged Higgs boson will mix to form four chargino eigenstates, $\chi_{1,2}^{\pm}$. Due to its quantum numbers the gluon will not mix and thus there is only one partner for each gluon, the gluino.

A listing of the particles in the MSSM is given in table 2.1.

## 2.4 Masses and symmetry breaking

As mentioned before, the superpartners should have identical masses to their corresponding SM particles. Experiments however place lower limits of 50-100 GeV. Their larger masses must originate from the mechanism that breaks

Table 2.1: List of MSSM particles, grouped the type of superpartner. Neutralino and chargino states are noted before and after electroweak symmetry breaking (EWSB)

| | Particle spin | | |
|---|---|---|---|
| | **0** | **1/2** | **1** |
| **Scalar** | $\tilde{q}^i_{L/R}$ | $q^i$ | - |
| | $\tilde{\ell}^j_{L/R}$ | $\ell^i$ | - |
| | $\tilde{\nu}^j_L$ | $\nu^j_L$ | - |
| **Neutralinos** | $h^0_u$ | $\begin{pmatrix} \psi_{h^0_u} \\ \psi_{h^0_d} \\ \lambda_0 \\ \lambda_3 \end{pmatrix} \overset{EWSB}{\Longrightarrow} \begin{pmatrix} \chi^0_1 \\ \chi^0_2 \\ \chi^0_3 \\ \chi^0_4 \end{pmatrix}$ | - |
| | $h^0_d$ | | - |
| | - | | $B^0$ |
| | - | | $Z^0$ |
| **Charginos** | $h^\pm$ | $\begin{pmatrix} \psi_{h^\pm} \\ \lambda^\pm \end{pmatrix} \overset{EWSB}{\Longrightarrow} \begin{pmatrix} \chi^\pm_1 \\ \chi^\pm_2 \end{pmatrix}$ | - |
| | - | | $W^\pm$ |

supersymmetry. As with the Higgs mechanism, it is assumed that this breaking occurs spontaneously, in order to preserve the underlying structure of the theory. Furthermore, there are no a priori constraints on the form of the breaking term, apart from that it should be soft, that is, preserving the regulating features of supersymmetry.

The most common way of parameterising supersymmetry breaking is to assume it happens in some hidden sector, meaning that the fields responsible for breaking supersymmetry are singlets under the $SU(3) \times SU(2) \times U(1)$ group of the SM or they are very heavy. Then some interaction or field is responsible for propagating this breaking to the fields of the MSSM, called the "messenger field". Different mediating fields have been proposed such as gravity-, gauge- and anomaly mediated supersymmetry breaking. This framework minimises the number of additional parameters imposed by supersymmetry breaking.

To describe the mechanism behind gravity mediation it is required to promote supersymmetry to a local symmetry. In doing this, gravity enters the theory, through the inclusion of a supermultiplet containing the spin-2 graviton and its spin-3/2 gravitino partner. Symmetry breaking is spontaneous, in a similar fashion to EWSB, described in section 1.4.3. While the precise mechanism of symmetry breaking is not very enlightening in its details, the aspect of gravitino mass is. Spontaneous symmetry breaking produces massless Goldstone bosons, or fermions for fermionic symmetries such as supersymmetry. In the case of local supersymmetry this Goldstone degree of freedom is absorbed by the gravitino to endow it with a longitudinal polarization and mass. In the end, the graviton remains massless as necessary, yet the gravitino acquires mass. The masses of the superpartners are then governed by this gravitino mass

scale, $m_{3/2}$, which is far lower than the Planck scale, $M_P$, where symmetry breaking occurs. This has the advantage of naturally producing superpartner masses at the TeV scale.

## 2.5 Cosmological considerations

Precise cosmological measurements, in particular those from the *Wilkinson Microwave Anisotropy Probe* (WMAP) indicate that out of the total density of the universe only 4.16% of matter is made up of baryons. A further 76.1% is made up of dark energy and 19.7% of *Dark Matter* (DM), these measurements are from combined WMAP and *Sloan Digital Sky Survey* (SDSS) data [7]. The DM component has to be some form of matter that is non-luminous. Neutrinos are already ruled out for this purpose as their mass is very small and their density is too low to cover the 19.7% budget.

From a cosmological point of view, new particle physics theories can be interesting as they introduce new particles that can form dark matter. This is possible in SUSY when R-parity is imposed. R-parity is a multiplicative symmetry and its quantum number is

$$R = (-1)^{3(B-L)+2s}\,. \tag{2.6}$$

This symmetry removes some proton decay terms from the Lagrangian and also constrains the decay modes of sparticles. In particular, annihilation and production occurs in pairs. A further consequence of this is that the lightest sparticle is stable and hence constitutes an excellent candidate for *Dark Matter* (DM). This particle is referred to as the *Lightest Supersymmetric Particle* (LSP). DM candidates need to be *Weakly Interacting Massive Particle* (WIMP), the currently favoured type of DM from astronomical and cosmological arguments. Therefore it must be electrically neutral to be a candidate. Furthermore, its present-day energy density should be in agreement with astrophysical observations.

In the early universe where the temperature was higher, sparticles would be produced abundantly. As the universe cools down these would decay with all these decay chains terminating with the LSP, if R-parity is respected. In the early universe the neutralino density is fixed at some equilibrium density $n_0$. At some later time the density $n$ changes as

$$\frac{dn}{dt} = -3Hn - \langle \sigma v_{rel} \rangle \, (n^2 - n_0^2) \tag{2.7}$$

The first term describes how the expansion of the universe affects the number of relics, where $H$ is the Hubble constant. The second term gives the contribution from relic annihilation, with cross-section $\sigma$ and relative velocity of

$v_{rel}$. For a high relic density annihilation will dominate, but as density drops, annihilation becomes less efficient. The temperature at which this happens is referred to as freeze-out temperature. This is commonly set to a temperature of $T_F = m_{relic}/20$. In order to calculate the present day relic density

$$n(T_0) = \frac{1}{m}\left(\frac{T_0}{T_\gamma}\right)^3 (T_\gamma)^3 \sqrt{\frac{4\pi^3 g_* G_N}{45}} \left[\int_0^{x_F} \langle \sigma v_{rel} \rangle \, dx\right]^{-1} . \tag{2.8}$$

Using this equation it is possible to calculate the relic density in the universe today and compare this with what astrophysicists measure as the DM density. It is noteworthy that for $\sigma = \sigma_{weak}$, using cross-sections that are of the order of magnitude of weak cross-sections, the relic density is at the same order of magnitude as required by cosmological constraints. This is a good test for supersymmetric models and very effectively excludes large regions of parameter space.

## 2.6 mSUGRA

The parameter space of the MSSM, 127 free parameters [9], is too large to be efficiently searched. To counteract this, theories have been developed that reduce the parameter space based on certain assumptions. One such model, *Minimal SUperGRAvity* (mSUGRA), is presented here with particular emphasis on the region of parameter space that concerns the analysis performed.

The mSUGRA model has only five free parameters, which is already a great improvement over the MSSM. It reduces the parameter space via a number of assumptions concerning the behaviour of the theory at the grand unification scale, $M_{\mathrm{GUT}}$. It is assumed that the masses of all scalar and fermion superpartners are unified to a common mass, $\mathbf{m_0}$ and $\mathbf{m_{1/2}}$ respectively. The ratio of the two Higgs doublet VEVs remains a free parameter, $\mathbf{tan}(\beta)$, as does the sign of the Higgs mass parameter, $\mathbf{sgn}(\mu)$. Finally, all trilinear couplings in the Lagrangian are assumed to take on a common value, $\mathbf{A_0}$.

The model is not quite so simple in the EW scale that LHC physics is concerned with. In order to get the masses of the superpartners at the EW scale the *Renormalization Group Equations* (RGEs) are used, to "run down" the parameters to energy scales lower than $M_{\mathrm{GUT}}$. In these equations the different couplings of the superpartners give contributions, which results in the superpartners acquiring different masses at the EW scale. To get a feeling for this, it can be said that gauge couplings drive the masses up, whereas Yukawa interactions lower them. It can be roughly said that:

- Because they interact strongly, the masses of squarks tend to be higher than leptons and neutralinos. Similarly for gluinos.

- Sleptons, since they do not interact strongly, get a lower mass than quarks, but they are usually heavier than the neutralinos.
- Neutralinos and charginos are usually the lightest class of sparticles in supersymmetric scenarios.
- Since left- and right-handed fermions differ in their hypercharge value there will be a mass difference between the two.

In practice, the exact mass hierarchy for the model is calculated using so-called SUSY spectrum calculators. The `isasusy` [10] calculator, is widely used in ATLAS for this purpose.

With these constraints it is possible to ask what phenomenological implications the model has and whether it is still viable. Most of the mSUGRA parameter space has already been excluded, primarily due to giving too high DM relic density and the LEP lower limit on the Higgs mass. The main regions shown in figure 2.2 still remain open and these are to be examined with the ATLAS detector.

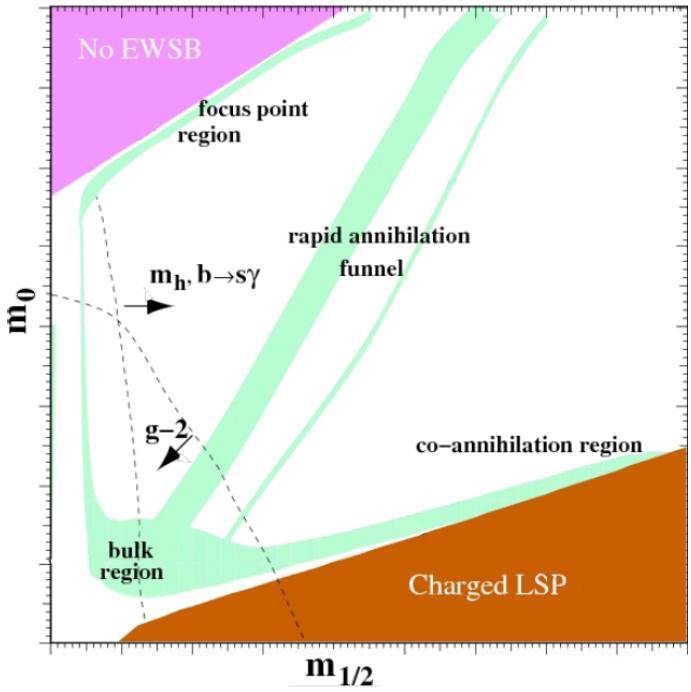


Figure 2.2: A plot of the allowed regions in mSUGRA parameter space. Light blue regions are allowed.

**The coannihilation region** is where there is a *next to lightest sparticle*, NLSP, that is almost mass degenerate to the LSP. The properties of this region will be discussed in detail further on.

**The bulk region** encompassing the low $m_0$ and $m_{1/2}$ part of parameter space is a typical region of mSUGRA, with neutralino self-annihilation through

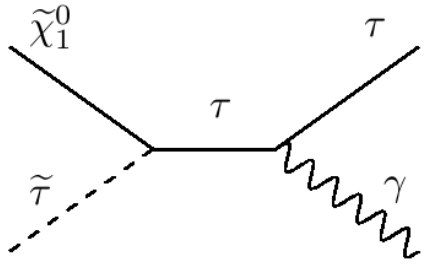


Figure 2.3: A diagram showing the coannihilation process in the SU1 region.

Table 2.2: The parameter set of the SU1 benchmark point.

| | | | |
|---|---|---|---|
| Unified scalar mass | $m_0$ | 70 | GeV |
| Unified fermion mass | $m_{1/2}$ | 350 | GeV |
| Common trilinear coupling | $A_0$ | 0 | GeV |
| Ratio of the two higgs VEVs | $tan\,(\beta)$ | 10 | |
| Sign of Higgs mass parameter | $sgn(\mu)$ | + | |

the slepton t-channel. WMAP measurements have recently constrained this region further, with only a strip currently allowed.

**The funnel region** is where LSP annihilation happens through heavy Higgs exchange, this process is further augmented with larger values of $\tan\beta$.

**The focus point** lies in the high $m_0$ regions and there the LSP is primarily higgsino-like. In this region neutralino self-annihilation is augmented through heavy vector boson exchange.

**Low mass region** Lastly, ATLAS also investigates a low mass region, with parameters producing small sparticle masses.

The so called SU1 benchmark point is located in the coannihilation region where the $\tilde{\tau}_1$ is the NLSP and is almost mass degenerate with the LSP. What this means is that the LSP annihilation cross-section is augmented through the $\tilde{\tau}_1$-$\tilde{\chi}_1$ annihilation channel, shown in figure 2.3, causing the present-day abundance of relic neutralinos to be in agreement with measurements by WMAP.

The SU1 benchmark point is defined by the parameters given in table 2.2. The mass spectrum as calculated by `Isasusy` is shown in table 2.3. As can be seen the squarks and gluinos that will be heavily produced in the LHC through the strong interaction have high mass and can then decay weakly into leptons and neutralinos.

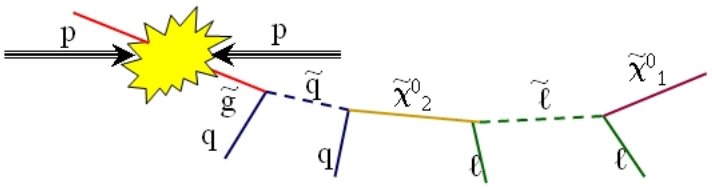


Figure 2.4: A typical decay chain in mSUGRA. Commonly initiated by gluon or a squark and further decays go through neutralino channels.

## 2.7 Experimental signatures

From an experimentalist point of view, SUSY has with many distinct signatures, if it exists at energies accessible to the LHC. The most prominent of these is the large missing energy. This is due to the escaping LSP that will carry large amounts of energy with it. This, however, has to be supplemented by more detailed study in order to pin-point the actual SUSY model manifested and its parameters.

### 2.7.1 Sparticle production

For a hadronic collider like the LHC the main production channels involve gluinos and squarks, since they interact strongly. For R-parity conserving scenarios, such as mSUGRA, these are pair-produced and the main production channels for sparticles are: $\tilde{q}\tilde{q}$, $\tilde{g}\tilde{q}$ and $\tilde{g}\tilde{g}$. Furthermore, the gluinos will further decay into squarks, which will be looked as the starting point of the cascade decays.

### 2.7.2 Topology of the cascade decays

Depending on the type of quark initiating the cascade the topology of the event can vary significantly. The following branching ratios (BR) for the decays are taken from [11], this is the output of `Isasusy` for the SU1 point.

Table 2.3: Masses of sparticles in the mSUGRA SU1 point, given in GeV.

| | | | |
|---|---|---|---|
| $\tilde{g}$ | 832.33 | | |
| $\tilde{u}_L$ | 760.42 | $\tilde{u}_R$ | 735.41 |
| $\tilde{d}_L$ | 764.90 | $\tilde{d}_R$ | 733.53 |
| $\tilde{b}_1$ | 697.90 | $\tilde{b}_2$ | 722.87 |
| $\tilde{t}_1$ | 572.96 | $\tilde{t}_2$ | 749.46 |
| $\tilde{\tau}_1$ | 146.50 | $\tilde{\tau}_2$ | 256.98 |
| $\tilde{\chi}_1$ | 136.98 | $\tilde{\chi}_2$ | 263.64 |

**Gluinos** decay with a 37% BR into light-flavour right-handed squark and 9.8% for light-flavour left-handed squarks. A further 44% is for decays to the heavy quark superpartners.

**Light flavour right-handed squarks** decay into a quark and LSP with a BR of 99%. These produce highly energetic jets.

**Light-flavour left-handed squarks** These will decay into a $\chi_2^0$ and a quark ( 31%) or a $\chi_1^\pm$ and a quark ( 60%). It is the former decay that interests us here.

**Heavy-flavour quarks** The light stop and sbottom have a 15% and 24% BR into the $\chi_2^0$ and a quark channel. The light bottom also has strong decay channels into $\chi_1^\pm$ and a quark ( 38%) and $\chi_2^\pm$ and a quark ( 23%). Light stops have similar decay channels with BRs of 47% and 14% respectively, but can also decay into $\chi_1^0$ and a quark (24%).
The heavy bottom partner has a 9.6% BR into the $\chi_2^0$ and a quark channel and 22% for the $\chi_1^0$ and a quark channel. A further 45% is for chargino channels.

Invariant mass distributions of cascade decay products are studied to extract SUSY masses. Since the LHC is a hadron collider and therefore the center-of-mass energy is not known at the parton level and the produced neutrralinos escape detection, it is the end-points of such distributions that are used. By measuring these end-points it is possible to determine relations between the SUSY masses. This is done for various combinations of particles. The end-point can be calculated theoretically as a function of sparticle masses. The theoretical expressions shown below are from [12]

The decay chain analyzed,

$$\tilde{q} \rightarrow q\,\chi_2^0 \rightarrow q\,\tilde{\tau}_1\,\tau^\pm \rightarrow q\,\chi_1^0\,\tau^\pm\,\tau^\mp \tag{2.9}$$

has a quark and two taus in its final state, plus the LSP that escapes detection.

The end-point of the invariant mass distribution of the two taus is expresses as

$$m_{\tau\tau}^2 = \frac{(m(\chi_2^0)^2 - m(\tau_2)^2)(m(\tau_1)^2 - m(\chi_1^0)^2)}{m(\tau_1)^2} \tag{2.10}$$

Using this expression and having measured the end-point a relation between the masses of different sparticles is obtained. In the case of the SU1 point studied, the theoretical end-point is at $m_{\tau\tau}^{max} = 82\text{GeV}$.

More complex combinations are possible as well. As mentioned, the chain is primarily started by a squark or gluino, which makes it possible to investigate the invariant mass of the quark and the two taus together. The end-point $m_{q\tau\tau}^{max}$ the end-point of the quark-tau-tau distribution has a theoretical value of

$$m_{q\tau\tau}^2 = \frac{\left(m(\tilde{q})^2 - m(\tilde{\chi}_2^0)^2\right)\left(m(\chi_2^0)^2 - m(\tilde{\chi}_1^0)^2\right)}{m(\chi_2^0)^2}\,. \tag{2.11}$$

Since the mass of the squark enters the equation, the end-point will depend on what squark initiated the cascade. The highest end-point would be produced when the chain is initiated by left-handed up and down squarks since they have the highest mass. From this expression its value is $m^{max}_{q\tau\tau} = 610\text{GeV}$.

The last two end-points are a combination of quark and a tau. The distribution containing the tau that originates from the $\chi^0_2$ decay and the squark is given by

$$m^2_{q\tau_{near}} = \frac{\left(m(q)^2 - m(\chi^0_2)^2\right)\left(m(\tilde{\tau}_1)^2 - m(\chi^0_1)^2\right)}{m(\tilde{\tau}_1)^2}\,, \tag{2.12}$$

and from the one from the stau decay

$$m^2_{q\tau_{far}} = \frac{\left(m(q)^2 - m(\chi^0_2)^2\right)\left(m(\chi^0_2)^2 - m(\tilde{\tau}_1)^2\right)}{m(\chi^0_2)^2}\,. \tag{2.13}$$

Making these distibutions depends on knowing which particle decay each tau originates from leads to these distributions being mixed together, making the determination of the end-point more difficult in these cases. The theoretical values of these end-points are $m^{max}_{q\tau_{far}} = 270\text{GeV}$ and $m^{max}_{q\tau_{near}} = 591\text{GeV}$.

# Chapter 3

# Experiment setup

The theory presented in the previous chapter requires particles at very high energies to be probed, since they will not make any contribution at low energies. The solution to this is to use colliders, machines that speed up particle beams and then collide them. The *Large Hadron Collider* (LHC), being built at CERN is used. To detect the products of the collisions and to test the predictions of proposed theories, detectors are built around the collision points in the accelerator. This study is based on the ATLAS detector (A Toroidal LHC ApparatuS).

## 3.1 LHC

The *Large Hadron Collider* (LHC) is a proton-proton synchrotron being built at CERN in Geneva. It has a nominal luminosity of $\mathcal{L} = 10^{34}\text{cm}^{-2}\text{s}^{-1}$ and 14 TeV *center of mass* (CoM) energy [13]. Alternatively the machine can accelerate and collide Pb ions beams for nuclear physics purposes. The machine resides in the tunnel of the LEP accelerator, decommissioned in 2000, and it is 27 km long.

The protons are injected in bunches with the LHC holding 2808 proton bunches with about $10^{11}$ protons each. The protons come from the pre-acceleration chain with an energy of 450 GeV and are accelerated in the LHC to an energy of 7 GeV. These two beams circulate within two separate bores, but within a common vacuum pipe, except for the interaction points where the beams cross. Bunch crossings occur every 25ns and an average of 19 interactions taking place in each crossing.

Four interaction points are set up for LHC, one for each of the major experiments. These are *ATLAS*, *CMS*, *ALICE* and *LHCb*. ATLAS and CMS are intended as general purpose experiments, whereas LHCb is oriented towards b-physics. ALICE on the other hand is focused on doing nuclear physics with Pb-Pb collisions. An illustration of the LHC accelerator, pre-acceleration chain and the four experiments is provided in figure 3.1.

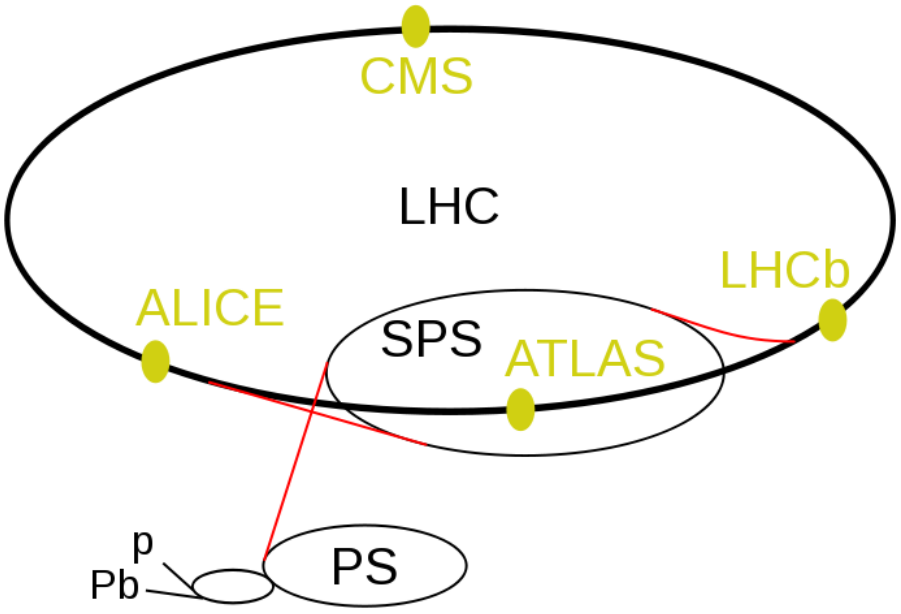


Figure 3.1: The LHC accelerator chain and the four experiments.

The start-up date of the LHC is now set to be August 9th with an initial luminosity of $\mathcal{L} = 10^{31}\text{cm}^{-2}\text{s}^{-1}$.

The luminosity for a storage ring can be calculated as

$$\mathcal{L} = \frac{fN^2}{4\pi\sigma_x\sigma_y}\,, \tag{3.1}$$

it depends on the frequency of the beams($f$), the cross-section of the beam($\sigma_x\sigma_y$) and the number of particles per bunch($N$). It has unit of ($b^{-1}s^1$). The luminosity gives a measure of the number of collisions that can be expected from the accelerator. As such it is a very important characteristic to define the performance of the accelerator. Luminosity integrated over time is referred to as intergrated luminocity and serves as a measure of the amount of data collected. The LHC will produce approximately $10fb^{-1}$ per year.

Having the cross-section for a given process to occur and the machine luminosity it is possible to calculate the rate of the process at the LHC by

$$N = \sigma \times \mathcal{L}_{LHC}\,. \tag{3.2}$$

## 3.2 ATLAS

The ATLAS detector is a general purpose experimental laboratory for the LHC, alongside the CMS. The general principles are that it should have good hermeticity, high energy resolution and excellent tracking. It consists of an inner detector, used for tracking, a calorimetry system to measure the energy of particles and a muon detector to track muons as they leave the calorimeter. The characteristics and performance of these components are presented below as well as remarks on the specific uses of these systems for particle physics.

### 3.2.1 Preamble

All information in this chapter is from ref [14], the ATLAS reference paper, to be published in the summer.

The coordinate system used in ATLAS is defined as follows:

- The x-axis points from the interaction point, towards the center of the LHC ring.
- The y-axis points upwards.
- The z-axis is along the beam direction.
- The azimuthal angle $\phi$ is defined by $\tan\phi = \frac{p_y}{p_x}$.
- The polar angle $\theta$ is defined as the angle to the beam axis.
- The pseudorapidity, $\eta$, is defined as: $\eta = -\ln(\tan\theta/2)$.

In general $\phi - \eta$ are used as coordinates. For angular separation the variable $R = \sqrt{\Delta\phi^2 + \Delta\eta^2}$ is used.

### 3.2.2 The inner detector

The inner detector (ID) in ATLAS is responsible for tracking. It is divided in three parts, the pixel and semiconductor tracker (SCT) and the transition radiation tracker (TRT). These parts can be seen in figure 3.2

**Pixel** The pixel detector is the main tracking device in ATLAS. It consists of three barrel layers of silicon pixels and three disks in the end-cap. Its coverage is $|\eta| < 2.5$. The resolution of the pixel detector is 10 $\mu$m in the $R - \phi$ plane and 115 $\mu$m in the $z$ or$R$ direction in barrel and end-cap respectively.

**SCT** The semiconductor tracker consists of three layers in the barrel and four end-cap disks and covers the $|\eta| < 2.5$ region. The resolution of the SCT is 17 $\mu$m in the $R - \phi$ plane and 580 $\mu$m in the $z$ or $R$ direction in barrel and end-cap.

**TRT** The transition radiation tracker is the outermost component of the ID. It is a straw tube detector that provides for most measurement points for tracking. It consists of 73 straw planes in the barrel and 160 planes in the end-cap. It covers the $|\eta| < 2.0$ region. Furthermore, electrons can

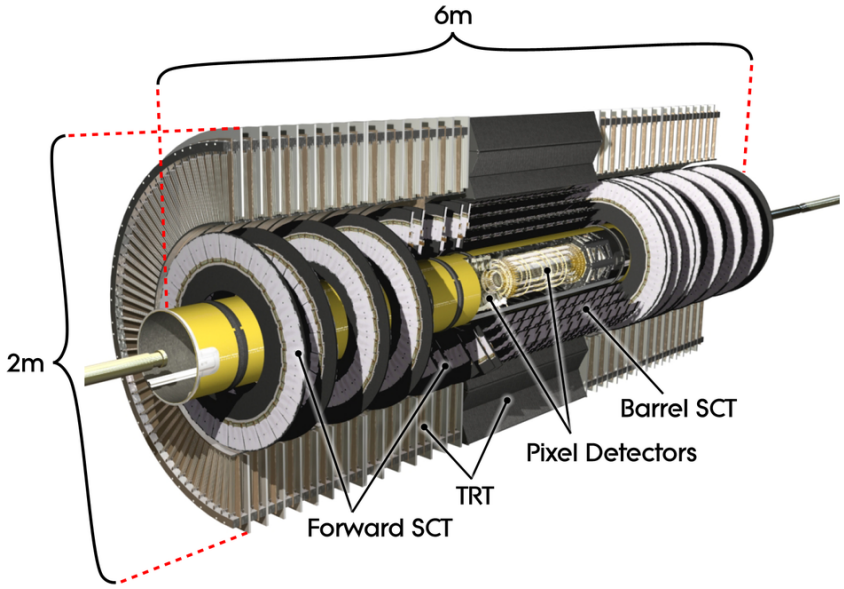


Figure 3.2: The ATLAS inner detector

be better identified by measuring the transition radiation they produce in the straws. This is possible for electron energies in the $0.5 - 150$ GeV range. The resolution of the TRT is 130 $\mu$m in both barrel and end-cap, but it can only provide $R - \phi$ information.

Table 3.1: Overview of the ATLAS tracking detectors.

| | | Accuracy | |
|---|---|---|---|
| **Detector** | **Coverage** | **R**$-\phi$ [$\mu$m] | **z** [$\mu$m] |
| Pixel | $\|\eta\| < 2.5$ | 10 | 115 |
| SCT | $\|\eta\| < 2.5$ | 17 | 580 |
| TRT | $\|\eta\| < 2.0$ | 130 | - |

### 3.2.3 The calorimeter system

The calorimeter system of ATLAS, responsible for measuring the energy of the produced particles consists of an electromagnetic and a hadronic calorimeter. These two systems and their subcomponents can be seen in figure 3.3.

**Electromagnetic calorimeter** The electromagnetic calorimeter is responsible for collecting the energy of electrons and photons. It is an inhomogeneous liquid Argon calorimeter. Its barrel part, housed inside the solenoid magnet cryostat, covers the $|\eta| < 1.475$ region. Two separate endcaps

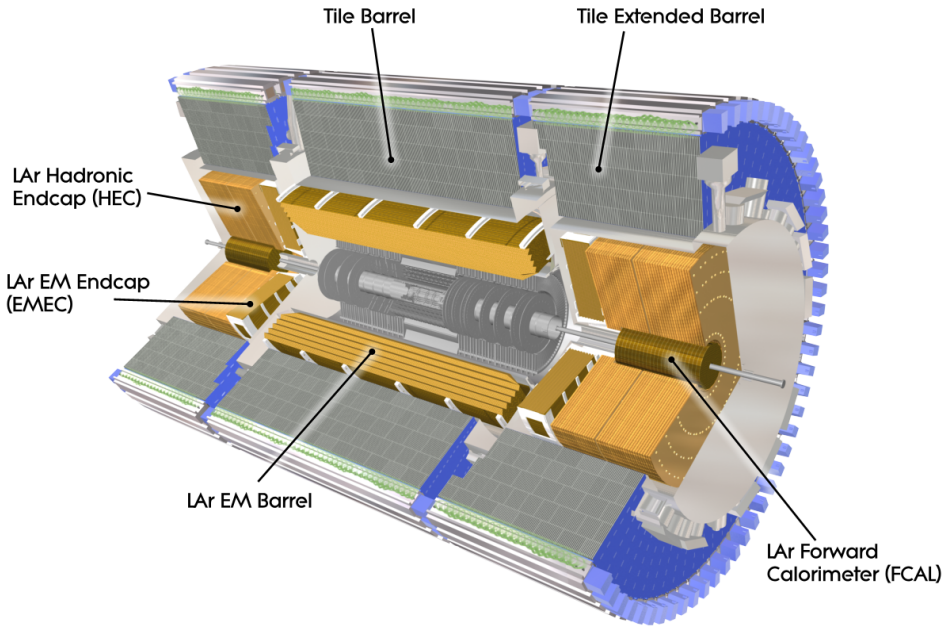


Figure 3.3: The ATLAS calorimetry setup.

Table 3.2: Overview of the ATLAS calorimetry system with projected resolutions.

| **Detector** | **Resolution** | **$\eta$-coverage** |
|---|---|---|
| EM calorimeter | $\sigma_E/E = 10\% \,/\, \sqrt{E} \oplus 0.17\%$ | $\pm 3.2$ |
| Had barrel/end-cap | $\sigma_E/E = 50\% \,/\, \sqrt{E} \oplus 3\%$ | $\pm 3.2$ |
| Had forward | $\sigma_E/E = 100\% \,/\, \sqrt{E} \oplus 10\%$ | $3.1 < \eta < 4.9$ |

provide high-$\eta$ coverage. The first endcap, the electromagnetic endcap (EMEC) covers the $1.375 < |\eta| < 2.5$ region, while the second forward endcap (FCAL) covers the $2.5 < |\eta| < 3.2$ region.

**Hadronic calorimeter** The hadronic calorimeter of ATLAS is a sampling calorimeter. Steel is used as the absorber with scintillating tiles as the active material. Due to this, it is also referred to as the tile calorimeter. It is separated into the barrel part and two extended barrels for high-$\eta$ coverage. The barrel covers the $\eta < 1.0$ region and the two extended barrels cover the region $0.8 < \eta < 1.7$. The main goals of the hadronic calorimeter are to provide good resolution in energy for hadrons as well as effective jet containment.

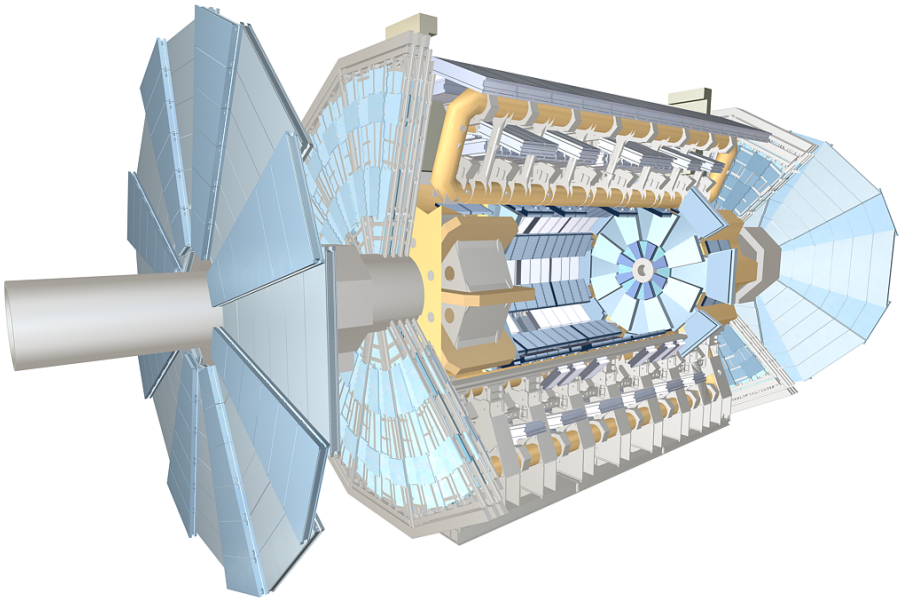

Figure 3.4: The muon spectrometer.

### 3.2.4 The muon spectrometer

By far the largest component of the ATLAS detector is the muon spectrometer. It's purpose is to detect muons and measure their momenta. To this end the whole muon spectrometer has a magnetic field throughout provided by the toroid magnets. The muon panels used to detect the passing of muons use four different detection methods, and separate chambers for precision measurements and triggering. An overview of the muon system is provided in figure 3.4.

**High precision chambers** The main type of detector for high precision measurements *Monitored Drift Tubes* (MDTs) are used for most part, whereas *Cathode Strip Chambers* (CSCs) are placed in the high $|\eta|$ region since they can withstand the higher particle flux and have higher granularity. The MDTs cove the $\eta < 2.0$ region whereas the CSCs cover the $2.0 < \eta < 2.7$ region.

**Trigger chambers** In the barrel region *Resistive Plate Chambers* (RPCs) are used for triggering and *Thin Gap Chambers* (TGCs) for the endcap. The trigger chambers cover the $|\eta| < 2.4$ region.

### 3.2.5 Magnet system

Momentum measurements can be performed using magnets to bend charged tracks. Two separate systems are used, the solenoid magnet in the ID region and the toroidal magnets for the muon spectrometer system. As charged particles transverse the parts of the detector with a magnetic field their tracks will be curved by the Lorentz force. The curvature of these tracks is determined by the charge of the particle and its momentum. This provides a momentum measurement, separate and complimentary to calorimetry information.

The solenoid magnet surrounds the ID. This superconducting magnet produces a uniform field of two Tesla. In order to minimize the material budget for the magnet it is placed in the same cryostat as the calorimeters.

The toroidal magnets are responsible for providing magnetic field in the muon system. There are eight air-core toroid magnets and two end cap magnets to provide magnetic field coverage in the high-$\eta$ regions. Due to this configuration it is not a uniform magnetic field, so a complex magnetic field map is required for physics analysis. The transition regions between the toroids and the end-cap are especially sensitive.

### 3.2.6 Putting it all together

With the above detectors it is possible to see most of the particles that interest us. As seen from the summary above, ATLAS does not provide any hadron identification detectors and therefore its capabilities in this area are rather weak. However, for the majority of subjects that it intends to delve into such capabilities are not required. Below is a list of objects ATLAS identifies as well as their signatures

**Electrons** leave a track in the ID, with high-threshold TRT hits if energetic enough, giving good identification. They are contained in the EM calorimeter, leaving an energy deposit there.

**Photons** are only seen through their energy deposit in the EM calorimeter.

**Muons** leave a track in the ID and interact very weakly in the calorimeters. They are not contained therein and reach the muon detectors, where they leave a track as they pass through. By determining how much the track bends in the magnetic field of the toroidal magnets a momentum measurement is extracted.

**Taus** can only be distinguished in their hadronic decay modes and are seen as narrow hadron jets. More information on their properties can be found in chapter 4.

**Hadron jets** are copiously produced in the LHC, as it is a hadron collider. They are seen as collections of many tracks in the ID, with heavy deposits in the calorimeters, particularly in the hadronic calorimeters. It is further possible to identify whether these jets come from a bottom quark

since in that case the jet will be seen to have a high impact parameter. Identification of such jets is referred to as b-tagging.

**Missing** $E_{\mathrm{T}}$**,** $\not{E}_{\mathrm{T}}$**,** is the collective imbalance of energy in the detector. It is only measured in the transverse direction, as the initial energy of the partons is not known in the z-direction. In the SM it is carried by neutrinos that escape detection, but for many *beyond the Standard Model* (BSM) scenarios large missing $E_T$ is the smoking gun signature, e.g. the LSP in supersymmetric scenarios. Uncertainties in calorimetry can also produce fake $\not{E}_{\mathrm{T}}$.

### 3.2.7 Triggering and data acquisition

The LHC bunch crossings will occur at a rate of 40 MHz, or once every 25 $\mu$s. This produces very high data rates as well as a challenge for electronics design. Most of these events are not of interest, as they originate from interactions of partons with low momentum. To counter this, a hierarchical trigger system is used. A set of measurements done by the detector are used to assess the interest of the event for physics. Its implementation in ATLAS is divided in three parts, level one (L1) and two (L2) and the event filter (EF). L2 and EF together make up the ATLAS high level trigger.

L1 is timed by the LHC clock. It uses readout from the muon trigger chambers and the calorimeters, but with decreased resolution. Its trigger menus are focused on detecting the presence of highly energetic objects or large amounts of missing energy. In fact all of the ATLAS physics objects are looked for at this early stage. If interesting features, labeled *regions of interest* (RoI), are identified in the event they passed on to the L2 trigger.

In the L2 trigger the ROI's identified by the L1 are further investigated. The L2 trigger then uses full granularity detector information to better assess the importance of the identified objects. After this step the trigger rate is lowered to 3.5 kHz. Last, the event is passed to the event filter, where the event is fully reconstructed using offline-like methods, albeit optimized for speed. Now the event is fully reconstructed and scanned for interesting features. At this point the event rate is reduced to 200 Hz and if an event passes the EF it is read out by the *Data AcQuisition* (DAQ) system and taken for bulk reconstruction.

### 3.2.8 Computing model

Even after the trigger selection, the data rate of the ATLAS detector remains prohibitively large for centralized storage at CERN. Instead, the data is reconstructed centrally at CERN and then pushed to the various computing centers with large amounts of storage.

In this system, the central node, CERN, is referred to as Tier 0, doing the basic reconstruction. The data is then pushed to eight main centers around the world

(Tier 1) that do further processing and store the data. Smaller centers exist (Tier 2) to provide additional storage and access for physics analysis.

Similarly, for physics analysis, the amount of computer power required is larger than can be provided by most participating universities. Therefore a framework is in place such that the computational power of participating institutes can be pooled together.

The framework used to satisfy these goals is referred to as the grid.

### 3.2.9 ATLAS Software

The software used by the ATLAS collaboration is built upon the `Athena` framework, which in turn uses to `Gaudi` [15] architecture. This framework is used for the complete simulation and reconstruction chain of ATLAS.

The collisions and resulting particles are simulated using *Monte Carlo* event generators. These use numerical methods to calculate the cross sections and the probability for the processes occurring. Two different ones are needed for the samples used for this work, `Pythia` [16] and `Herwig` [17]/`Jimmy`. `Pythia` is used for the SM samples whereas `Herwig` with the `Jimmy` interface are used for the SUSY samples.

Following event generation, `GEANT` takes over, to simulate the passage of the resulting particles through the detector and their interactions with it. Using this information digitization is then carried out to calculate what the response of the detector to these particles will be and produce data that would approximate the output of the detector during real collisions. After this step a *raw data object* (RDO) file is produced.

Reconstruction is the final step and it involves deducing what particles produced the output seen in the detector. The different objects mentioned in 3.2.6 are reconstructed with different packages running within `Athena`. The reconstruction algorithms that are relevant to the analysis work are presented in the next chapter.

Data production has been done on a large scale for the *Computer Systems Commissioning* (CSC) data challenge. During this data challenge data samples were defined by the ATLAS collaboration and then centrally produced and validated in the production system.

# Chapter 4

# ATLAS reconstruction

Reconstruction is the proces by which the objects in section 3.2.6 are identified by their signals in the detector. The algorithms that reconstruct the objects used for analysis will be briefly discussed here. These are tau, jet and missing transverse energy reconstruction. Special attention is given to the tau reconstruction algorithms as taus are the main probe of the study.

## 4.1 The tau lepton

Taus are the heaviest leptons and constitute the main probe of this study. Since they are so short lived ($\tau_\tau = 2.90 \times 10^{-13}$s) they have to be identified and reconstructed by their decay products. Because of high mass ($m_\tau = 1776.99 \pm 0.29$MeV) taus can decay both hadronically and leptonically.

### 4.1.1 Topology of tau decays

In order to understand how tau reconstruction proceeds, it is vital to get an understanding of the topology of tau decays. The following is a brief overview, with information from the Tau CSC note [18], where Therese Sjursen and myself contributed.

The decay of the tau is mediated by the weak interaction, meaning a tau neutrino always accompanies the decays. In the case of hadronic decays it is predominantly charged and neutral pions that are seen in the final state.

**Leptonic** decay modes are of the form: $\tau \rightarrow \ell\, \nu_\ell\, \nu_\tau$. The small lifetime of the tau makes it very challenging to distinguish these decays from primary electron or muon production. Furthermore, the presence of two neutrinos in the final state means more momentum is lost in these modes.

**Single-prong hadronic** decay modes are the ones used here predominantly. They are of the form: $\tau \rightarrow h^{\pm} n\, h^0 \quad n = 0, 1, 2, 3....$ These modes are the easiest to reconstruct, the charged hadron leaves a track in the ID that can be used as a seed and the neutral pions, leave a strong signature in the electromagnetic calorimeter.

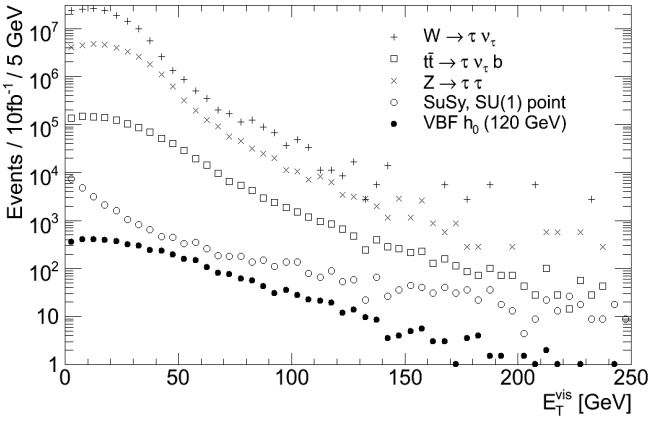


Figure 4.1: Distribution of $E_T$ for taus from different processes.

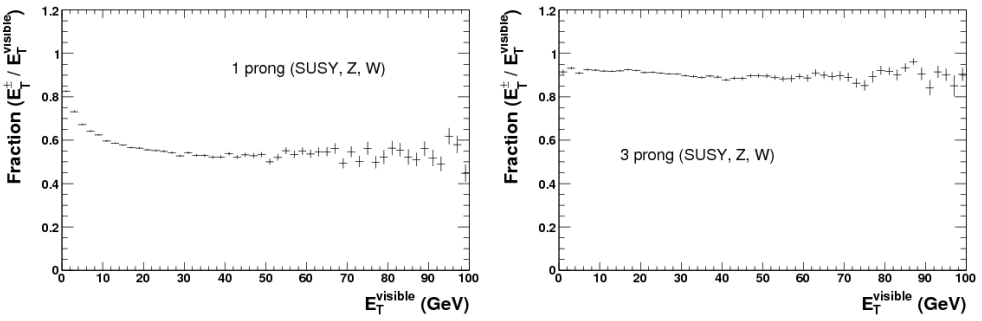


Figure 4.2: The fraction of the energy going into charged decay products, for single-prong(left) and three-prong(right) taus.

**Three-prong hadronic** decay modes, $\tau \to 3h^{\pm} n\ h^0 \quad n = 0, 1, 2, 3...$, are also good to reconstruct, but due to the higher multiplicity in charged tracks, rejection against jets is harder.

A summary of the most important decay modes are given in table 4.1, including the BR's for the various decay modes. A complete table can be found in [3].

Having few tracks hadronic tau decays look like very narrow jets. Coupled with the fact that the dominant $\pi^0$ (98.8%) decay channel is $\pi^0 \to \gamma\,\gamma$ [3], these will give high deposits in the EM calorimeter. This and the low track multiplicity make tau-jets distinguishable from QCD jets. Tau reconstruction exploits these features. Energy distribution between charged and neutral particles can be found in figure 4.2. It can be seen that the amount of charged and neutral energy differs significantly between the single- and three-prong case.

Table 4.1: The BRs for the decay modes of taus

| Mode | BR |
|---|---|
| $\mu^+\bar{\nu}_\mu\nu_\tau$ | $(17.36 \pm 0.05)\%$ |
| $e^+\bar{\nu}_e\nu_\tau$ | $(17.84 \pm 0.05)\%$ |
| $h^+\,\nu_\tau$ | $(10.90 \pm 0.07)\%$ |
| $h^+\,(\geq 1\,h^0)\,\nu_\tau$ | $(37.05 \pm 0.12)\%$ |
| $\pi^+\nu_\tau\cdots$ | |
| $\cdots\,\pi^0$ | $(25.50 \pm 0.10)\%$ |
| $\cdots\,\pi^0\pi^0$ | $(9.31 \pm 0.12)\%$ |
| $\cdots\,\pi^0\pi^0\pi^0$ | $(1.17 \pm 0.08)\%$ |
| $h^+h^+h^-\,\nu_\tau$ | $(9.33 \pm 0.08)\%$ |
| $h^+h^+h^-\,(\geq 1\,h^0)\,\nu_\tau$ | $(14.59 \pm 0.08)\%$ |
| $\pi^+\pi^+\pi^-\nu_\tau\cdots$ | |
| $\cdots\,\pi^0$ | $(4.59 \pm 0.07)\%$ |
| $\cdots\,\pi^0\pi^0$ | $(5.02 \pm 0.34)\%$ |
| $\cdots\,\pi^0\pi^0\pi^0$ | $(1.17 \pm 0.08)\%$ |

## 4.2 Tau reconstruction

Two algorithms exist for tau reconstruction in ATLAS, `tau1p3p` and `tauRec`. The primary difference between the two algorithms is which of the two tau signatures is used as seed. `Tau1p3p` starts with tracking information whereas `tauRec` starts with collecting calorimetry information. Their workings are presented here, with an emphasis on `tau1p3p` as that is the one used in the analysis presented in chapter 5.

### 4.2.1 Calorimeter clusters

The energy deposits of taus are organised into clusters using topogical clustering [19]. This algorithm works by clustering together energy deposits based on the amount of energy deposited in neighbouring cells. The algorithm can be configured to run using different parts of the calorimeter system.

### 4.2.2 Tau1p3p

The track based package in `Athena` is called `tau1p3p`. It is track based in the sense that it uses tracks left by the charged particles in the inner detector as its seeds. Then these tracks are matched to corresponding energy deposits in the calorimeters.

To begin reconstruction a leading track is identified. It must be above a certain energy threshold (9 GeV) as well as be of good quality, given by its number of hits in straw and silicon detectors and a minimum value on the impact parameter and $\chi^2$ of the fit. For three-prong taus also two more charged tracks are

taken around the leading track in a cone of $\Delta R = 0.2$. The barycenter, weighted by momentum, of these tracks acts as the seed in this case.

Having the initial seed the algorithm then extrapolates into the calorimeters and collects energy deposits in the EM calorimeter in $\Delta R = 0.2$ cone. The energy scale of the candidate is defined as:

$$E_T = E_T^{emcl} + E_T^{neuEM} + \sum p_T^{trck} + \dots , \tag{4.1}$$

where the $E_T^{emcl}$ term contains all energy deposits in the EM calorimeter with no corresponding hadronic deposit, the $E_T^{neuEM}$ term includes neutral electromagnetic energy (here coming from $\pi^0$s) and the last term adds the momenta of the tracks. More information can be found in [20].

From the above tau candidates are formed. These have to be further identified, i.e. be verified as good taus. This is done using various observables such as:

**Electromagnetic radius,** $R_{em}$ is formed by taking the distance between the candidate's seed and energy deposits in the EM calorimeter, weighted by their energy:

$$R_{em} = \frac{\sum \Delta R^{\tau,cell} E_T^{cell}}{\sum E_T^{cell}} . \tag{4.2}$$

**Deposits in strips,** $N_{strips}$ is the number of strips with an energy deposit above a certain threshold

**Width of energy deposition,** $W_{strips}$ in strips is the variance of energy deposition in $\eta$ weighted by the energy deposits.

**Fraction of energy in** $0.1 < \Delta R < 0.2$ **cone,** $frac_T^{R12}$ is the fraction of energy in the $0.1 < \Delta R < 0.2$ region of the core.

**Energy deposits in the halo region,** $E_{halo}$ is the amount of energy deposited in the halo region, $0.2 < \Delta R < 0.4$.

**Number of tracks** for the candidate.

**Invariant mass** of tracks, if more than one.

Different jet rejection schemes have been set up using the discrimination variables such as cuts, neural networks, PDERS (Probability Density Estimator with Range Searches) and likelihood ratio.

### 4.2.3 TauRec

The alternative method to the above, used in the `tauRec` algorithm [21], is to look for calorimetric clusters and correlate these with tracks in the inner detector. In this scenario, a circle of size $\Delta R = 0.4$ is used, within which all topological clusters are collected. Using this as a seed, tracks in the inner detector, lying within a cone of $\Delta R < 0.3$ and passing certain quality criteria are grouped. These include the quality of the tracks, their number and charge. As above

only one- and three-prong candidates are considered and the charge should add up to $\pm e$.

Within the `Athena` framework, both of these algorithms are included in the TauRec package and are run during reconstruction. Due to the focus on low-energetic taus the `tau1p3p` alorithm is chosen for tau reconstruction for the rest of the analysis.

## 4.3 Algorithm merging

Starting with `Athena` release 14.0.0, the two tau algorithms are merged into a single package providing both methods if possible [22].

The algorithm starts by collecting tracks that can be used as `tau1p3p` seeds as well as suitable topological clusters. The tracks are looped over and used for `tau1p3p` reconstruction. Tau candidates reconstructed this way are then propagated into the calorimeters to check whether a topological cluster matches to it. If so `tauRec` recontruction is run with the cluster as seed. In the last step remaining clusters are used for `tauRec` reconstruction.

This procedure produces candidates that may be `tau1p3p`, `tauRec` or overlapping candidates.

One important change of relevance for this study is the lowering of $p_T$ threshold for the seeding track of `tau1p3p` to 6 GeV. This means that more candidates can be reconstructed in the low momentum region that is of interest in the coannihilation region.

## 4.4 Tau Identification

Identification is done according to the suggestions layed out in [23]. For `tau1p3p` candidates the *efficNN* neural network is chosen with a moderate rejection on jets. Two veto flags are in place to discriminate against electrons and muons. For `tauRec` candidates two likelihood distributions are used against jets and electrons. Furthermore both candidates from both algorithms need to have a charge of $\pm 1$ to be accepted. An overview of the identification criteria is presented in 4.2.

### 4.4.1 Overlap removal

After taus are identified it is also useful to perform "overlap removal", that is to check that different reconstruction algorithms do not identify the same object. In the case of taus it is most important to remove overlap with electrons, as they share many characteristics. Any tau that is also identified by the electron

Table 4.2: Variables used for tau identification for tauRec and tau1p3p. On the left are the cuts used for the samples reconstructed with release 14.1.0.2 and using the merged algorithm. On the right are the cuts when using the 12.0.6 release reconstruction done for the CSC with tau1p3p.

| | **Observable** | **14.1.0.2** | **12.0.6** |
|---|---|---|---|
| **Tau1p3p** | EfficNN | $> 0.3$ | - |
| | DiscCut | - | $= 1$ |
| | Charge | $\pm 1$ | |
| | Pseudorapidity | $\|\eta\| < 2.5$ | |
| | No electron or muon veto | | |
| **TauRec** | Likelihood(Jets) | 4.0 | - |
| | Likelihood(Electrons) | 1.6 | - |
| | Charge | $\pm 1$ | - |
| | Pseudorapidity | $\|\eta\| < 2.5$ | - |

algorithm is removed, since electron efficiency is higher. The same procedure is followed for muons. Similarly jets that are also identified as taus should be removed.

## 4.5 TauMerged performance

In order to consider the performance of the algorithm two quantities are considered as benchmark, the efficiency and the purity. The efficiency is

$$\epsilon = \frac{\text{\# of true } \tau \text{ matched to identified } \tau}{\text{\# of true } \tau} \tag{4.3}$$

whereas the purity is defined as

$$p = \frac{\text{\# of identified } \tau \text{ matched to true } \tau}{\text{\# of identified } \tau} \tag{4.4}$$

Figure 4.3 shows the number of reconstructed taus and true taus as a function of transverse momentum. The efficiency of the reconstruction can be found in figure 4.4 as a function of tau momentum. As can be seen at the low-$p_T$ regions that are of interest the efficiency is very low. The optimal region lies in 20-70 GeV with an efficiency higher than 30%.

For a comparison to using only `tau1p3p` the efficiency using the tauID requirements for `tau1p3p` shown in table 4.2 is plotted in figure 4.6. By comparing it to figure 4.4 it is seen that the efficiencies are very similar for the two samples. For the purity however, in figures 4.5 and 4.7 an improvement can be seen using the merged reconstruction procedure, although due to low statistics it is hard to give an accurate estimate of how much improvement there is. Such

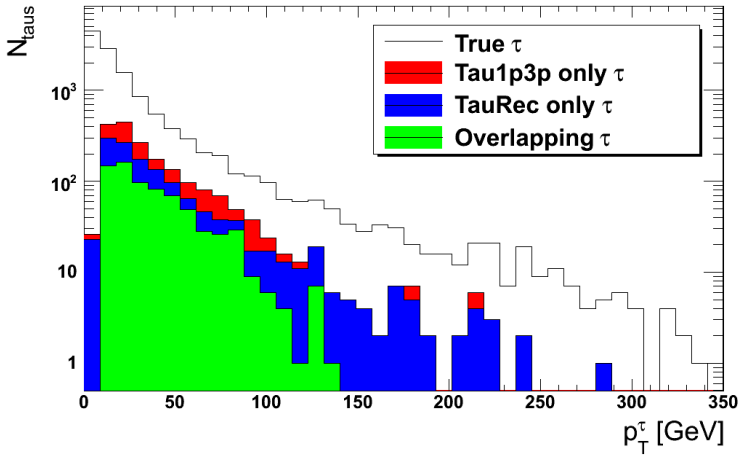


Figure 4.3: The number of reconstructed taus in the sample. Taus reconstructed by one of the two methods exclusively are shown as well as the overlap candidates. Number of true taus shown for reference. Sample 5401 with 14.1.0.2 reconstruction.

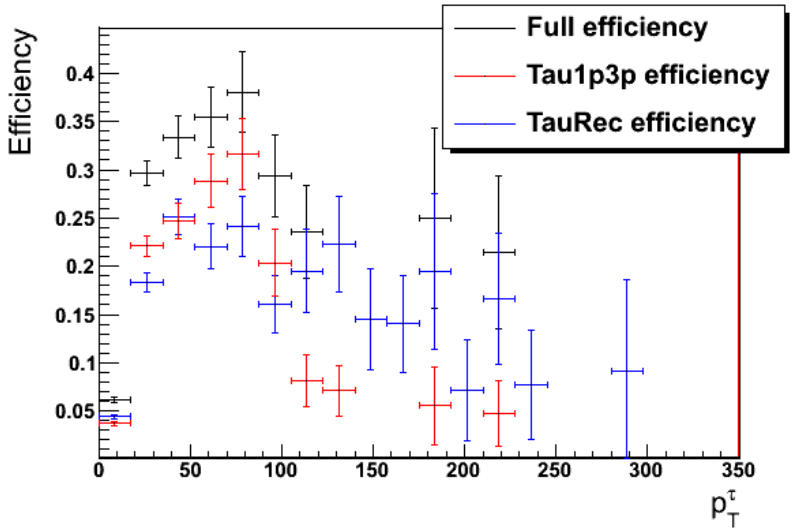


Figure 4.4: The efficiency of the reconstruction as a function of $p_T$. Shown are separately the efficiency of the algorithm as a whole and for the two different methods. Sample 5401 with 14.1.0.2 reconstruction.

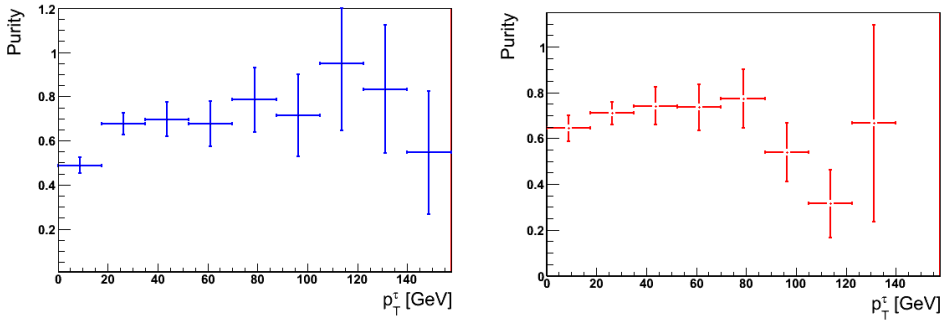


Figure 4.5: Purity of reconstructed taus as a function of momentum. `TauRec` (left) and `tau1p3p` (right) shown separately. Sample 5401 with 14.1.0.2 reconstruction.

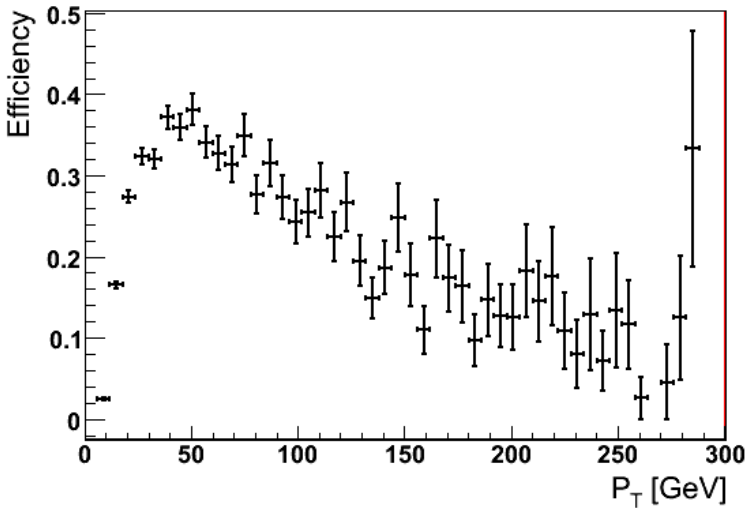


Figure 4.6: The efficiency of the reconstruction using `Athena` version 12.0.6 as a function of $p_T$. Sample 5401.

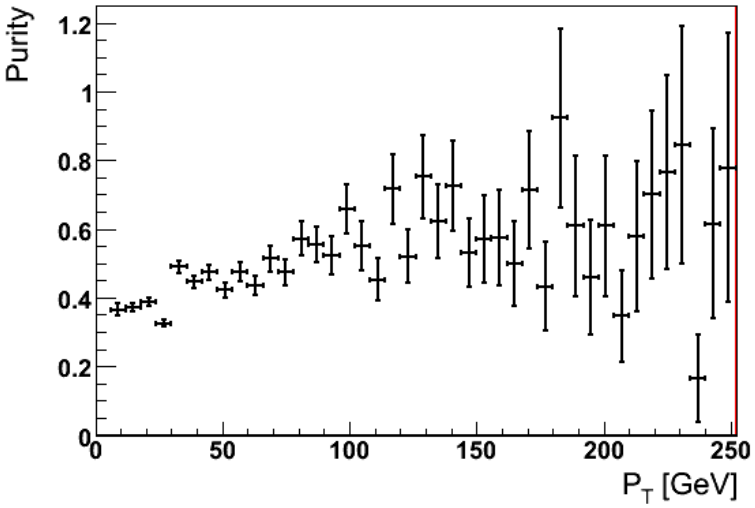


Figure 4.7: The purity of the reconstruction using `Athena` version 12.0.6 as a function of $p_T$. Sample 5401.

improvement can be expected however due to the hardening of the tau identification criteria in the merged mode sample and comes at no noticeable cost in efficiency.

Another evaluation of `tau1p3p` performance is shown in [24].

## 4.6 Jet reconstruction

In ATLAS two types of jet reconstruction algorithms are used, the cone and $k_T$ algorithms. They work on the topological clusters defined earlier and group them together to form jets. The cone algorithm is used in the analysis, as suggested in [25]. The algorithm works by using high-$E_T$ particles as seeds and for reconstruction. A cone is placed around the seed and all particles within it are collected into the jet. Two cone sizes are used in ATLAS, $\Delta R = 0.4$ and $\Delta R = 0.7$. For SUSY analysis 0.4 is preferred. The "center" of the jet is then recalculated. If it is further from the current center of the cone than some preset value another iteration takes place with the cone placed in the new center. The algorithms use H1-style calibration [26].

## 4.7 Missing transverse energy reconstruction

Missing transverse energy ($\not{E}_T$) in ATLAS is calculated in different ways. For physics analysis purposes *MET_EtMissRefFinal* is used which is defined as the scalar sum of the $E_T$ of

**Electrons/Photons.**
**Calorimeter cells** that belong to jets, H1-calibrated [26].
**Topological clusters** that fall outside reconstructed jets, H1 calibrated [26].
**Muons** reconstructed with the Staco (see chapter 8 in [27]) algorithm.

These are summed in the X and Y direction and transverse energy imbalance determined from them.

# Chapter 5

# Analysis

In this chapter an analysis of SUSY events in the SU1 benchmark point is presented. First a background rejection method is described, one of many done in collaboration with Therese Sjursen. The method proves successful but additional background statistics are necessary to optimize further. Following this invariant mass distributions fromt he visible decay products of the decay chain $\tilde{q} \rightarrow q\tilde{\chi}_2^0 \rightarrow q\tilde{\tau}_1\tau^{\pm} \rightarrow q\tilde{\chi}_1\tau^{\pm}\tau^{\mp}$ are analysed and end-points determined from their distributions. Two different samples were used for this part, the full CSC dataset of SU1 events as well as a smaller 20000 event AOD sample reconstructed from CSC RDOs with `Athena` release 14.1.0.2. The full CSC data are used for the first tau-tau end-point while the AOD sample is used in order to conclude on how jets and taus should be selected for the distributions involving the jet originating from the squark in the decay chain.

## 5.1 Sample definitions

All the samples used in the analysis, were produced for the CSC, see section 3.2.9, data challenge and produced using the ATLAS production system. The samples used are

**5401** is the signal sample for this analysis. It contains sparticle production events in the SU1 point of mSUGRA, see section 2.6.

**5200** is the primary background, containing top-antitop production events, that closely mimic the signal characteristics.

**5188** contains Z production with forced leptonic decays.

**5107** contains W production with forced leptonic decays.

A second signal sample was made for this study using the RDO's, see section 3.2.9, produced in the CSC for sample 5401 and reconstructing them privately. Reconstruction used `Athena` release 14.1.0.2 and the merged tau reconstruction algorithm, as described in section 4.3, to evaluate its potential for coannihilation region studies.

Table 5.1: Cross sections and sample size for signal and backgrounds.

| Process | Sample | X-section (pb) | Version | # of events |
|---|---|---|---|---|
| SU1 | 5401 | 11.46 | 12.0.6 | 198 600 |
| | | | 14.1.0.2 | 20 000 |
| $t\bar{t}$ | 5200 | 461 | 12.0.6 | 349 800 |
| $Z \rightarrow \tau\bar{\tau}$ | 5188 | 246 | 12.0.6 | 149 200 |
| $W \rightarrow \tau\bar{\nu}_\tau$ | 5107 | 5536 | 12.0.6 | 338 700 |

The cross-sections of these samples and the `Athena` version used for reconstruction are summarized in table 5.1.

## 5.2 Backgrounds

The main backgrounds considered in this study are

$t\bar{t}$ **production,** where the tops decay as $t \rightarrow W\,b \rightarrow \tau\bar{\nu}_\tau\,b$. If both tops produced go through this process the resulting event very closely mimics the cascade decays of SUSY and is the most difficult background to reject.

**W and Z production,** where both the Z and the W can decay through tau channels.

**QCD jets,** are produced heavily and with great cross-sections. However $\not{E}_T$ is not commonly associated with such events making it easy to reject such events with very high efficiency. These are therefore not considered further.

As seen in table 5.1 the cross-sections for the background samples are an order of magnitude higher than for the signal. It is therefore essential to have a strong background rejection strategy in place. Many different strategies were looked into, a complete listing of these methods can be found in Therese Sjursen's thesis [28]. Only one of them will be presented here.

Two quantities that are characteristic of SUSY events are used in this method, the presence of highly energetic jets and large $\not{E}_T$. The energy of the jets and $\not{E}_T$ are then correlated and an elliptic cut is applied on them, i.e. rejecting events with both low missing $\not{E}_T$ and jet energy. The parameters of the background rejection are the length of the semi-major and semi-minor axes of the ellipse.

The metric for the success of this selection is given by the sensitivity achieved through it. The latter is defined as

$$S = \frac{N_{\text{signal}}}{\sqrt{N_{\text{bg}} + N_{\text{signal}}}}\,. \tag{5.1}$$

The value of the sensitivity for various choices of the parameters can be found in table 5.2. As it is dependent on the number of events selected, it varies with integrated luminosity. The sensitivities in the table are calculated for 30fb$^{-1}$ integrated luminosity. From the point of view of sensitivity the optimum choice is to use the largest parameters shown in the table for the cut. On the other hand it is important to retain a large enough amount of signal to be able to extract useful information from it.

This elliptic cut method proves to be quite efficient, while remaining relatively simple to implement. A substantial amount of background is not rejected by the cuts however. To make background rejection stronger the cuts need to be stricter, but background statistics do not allow this, since there is a minimal amount of events left in the background samples. This can possibly be fixed by adding more events from fast simulated samples, though this was not done here, but is a possibility to further tune the background rejection parameters.

## 5.3 Invariant mass distributions

The invariant mass distributions discussed in section 2.7.2 contain information on the sparticle masses. In what follows these end-points are determined from simulated ATLAS data, both on generator and from reconstructed level. The tau-tau end-point is done with the 12.0.6 sample, with full statistics. For the end-points involving quarks the smaller 14.1.0.2. sample is used to determine which objects should be used for the invariant mass distributions and their end-points.

### 5.3.1 SUSY as background to itself

In addition to the backgrounds described above there are two more cases that are important. Jets in the event can be mistagged as taus creating false tau pairs in the event. Also, another SUSY cascade can produce a tau that is completely unrelated to the cascade decay that is sought after here.

For jets mistagged as taus there is an equal probability of their charge being reconstructed as positive or negative. The effect of this is that the $\tau\tau$ with a mistagged jet there is an equal probability that both taus have same sign (SS) and opposite sign (OS). It is therefore possible to remove this background by subtracting the SS distribution from the OS distribution.

If the taus originate from a different SUSY decay chain than the one investigated here the resulting tau pairs will usually have OS without any corresponding contribution to the SS pairs, making the above method of removing such background unusable. If two unrelated processes contribute taus, OS-SS subtraction can still work to some extent.

The contributions from these backgrounds can be seen in figure 5.1.

Table 5.2: The number of events passing the $E^{jet1} + E^{jet2}$ versus $\not{E}_T$. Shown are number of events passing from the samples as well as the number normalized to $30\,\text{fb}^{-1}$, shown in parenthesis. The sensitivity is shown, using definition (5.1).

| | **Missing $E_T$** | | | | | |
|---|---|---|---|---|---|---|
| $\sum_2$ **$E^{jet1}$** | **200 GeV** | **S** | **250 GeV** | **S** | **300 GeV** | **S** |
| **350 GeV** | 464/ 76/ 31 (519/3002/1503) | 7.56 | 450 / 58/ 25 (504/1291/2211) | 8.21 | 433/ 51/ 23 (488/2030/1115) | 8.33 |
| **400 GeV** | 455/ 57/ 22 (509/2251/1067) | 8.48 | 438 / 44/ 14 (491/1738/678) | 9.32 | 422/ 38/ 13 (473/1501/630) | 9.50 |
| **450 GeV** | 451/ 48/ 31 (505/1869/776) | 9.19 | 428 / 38/ 11 (479/1501/533) | 9.77 | 409/ 31/ 9 (458/1225/436) | 10.16 |
| **500 GeV** | 445/ 42/ 14 (498/1659/678) | 9.59 | 417 / 33/ 6 (467/1303/291) | 10.44 | 390/ 21/ 6 (436/830/261) | 11.28 |
| | **Missing $E_T$** | | | | | |
| $\sum_2$ **$E^{jet1}$** | **350 GeV** | **S** | **400 GeV** | **S** | **450 GeV** | **S** |
| **350 GeV** | 429/ 29/ 23 (480/1937/1115) | 8.35 | 422 / 44/ 20 (473/1738/969) | 8.65 | 409/ 40/ 20 (458/1580/969) | 8.63 |
| **400 GeV** | 412/ 32/ 12 (461/1265/582) | 9.86 | (398 / 29/ 12) (446/1146/582) | 9.83 | 384/ 26/ 11 (430/1027/533) | 9.91 |
| **450 GeV** | 388/ 24/ 8 (434/948/388) | 10.56 | 356 / 22/ 8 (409/869/388) | 10.28 | 356/ 22/ 8 (399/869/388) | 10.04 |
| **500 GeV** | 367/ 15/ 6 (411/442/291) | 11.69 | 352 / 13/ 5 (494/513/248) | 11.88 | 328/ 12/ 4 (367/474/194) | 11.64 |

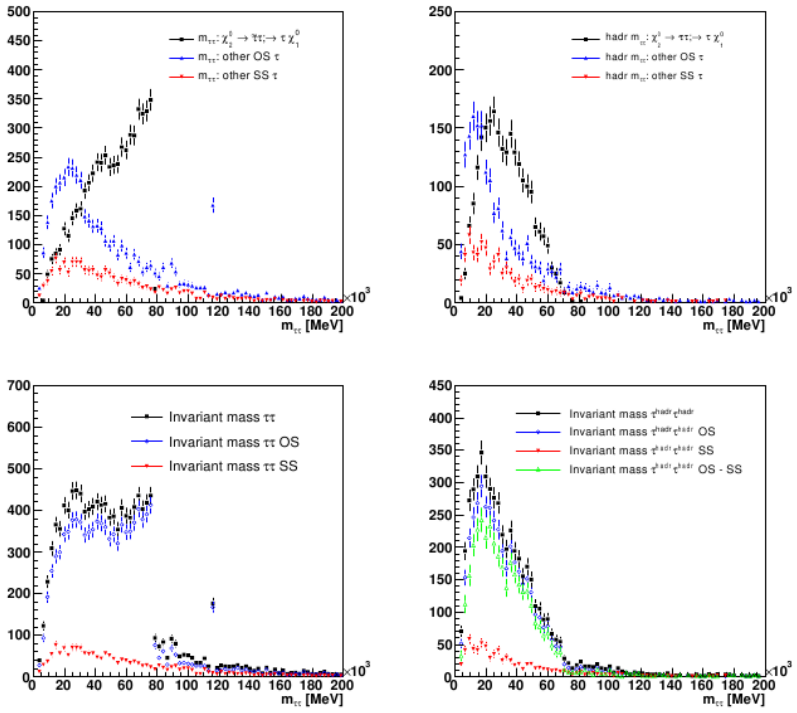


Figure 5.1: Distribution of OS and SS tau pairs done using truth information. In the upper left depicted is the distribution from the signal process, other OS pairs and SS pairs. In the lower right shown are all the OS and SS pairs together. The plots on the right hand side are similar but having taken only the visible energy into account. The figures are taken from [24].

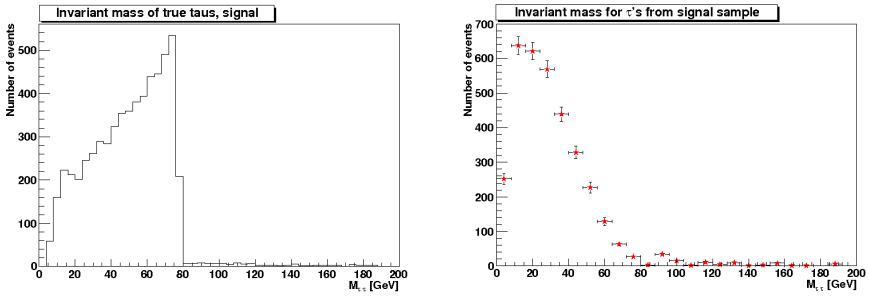


Figure 5.2: The tau-tau end-point, using generator information. On the left is the distribution as it looks by taking the tau energies, including the neutrino. On the right one can see how these change when only visible energy is taken into account, that is without the energy lost by the neutrino.

### 5.3.2 The $\tau\tau$ end-point

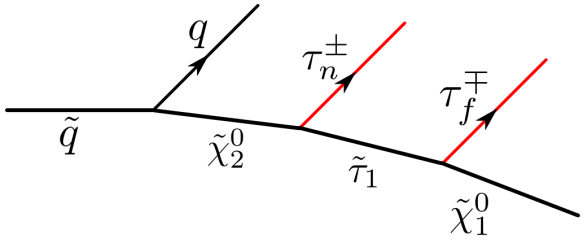


The tau-tau invariant mass distribution, seen from generator level information is plotted in figure 5.2. In the left plot the triangular shape of the distribution should be noted, with a hard cut-off at the end-point. Due to the escaping neutrino, the shape of the distribution changes as seen in the right plot, with the whole distribution shifting to the right and the end-point is no longer seen as clearly.

In order to obtain the end-point of such a distribution, two methods are considered. One is to perform a linear fit at the end of the distribution and the other is to fit using a function that follows the form of the distribution, the one used here was originally made for SU3 data in [29], and defined as

$$f(x) = \frac{p_0}{x} \cdot exp\left(-\frac{1}{2p_2^2}(ln(x) - p_1)^2\right) . \tag{5.2}$$

Using this function has the advantage of not relying too much on the range where the fit is performed.

As the function approaches the x-axis asymptotically it is the inflection point (IP) of the distribution that is used to determine the end-point. From the parame-

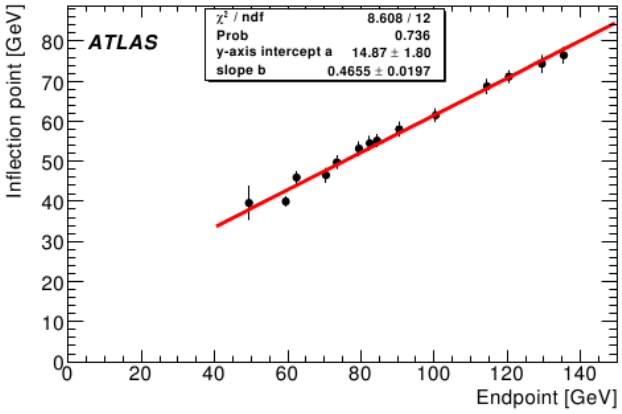


Figure 5.3: The calibration plot used to extract the end-point from the inflection point. The figure is taken from [29].

ters of the fit it can be derived as

$$m_{IP} = exp\left(-\frac{1}{2}p_2^2\left(3-\sqrt{1+\frac{4}{p_2^2}}\right)+p_1\right)\,. \tag{5.3}$$

A calibration has been done to determine the relation between the IP and the end-point of the distribution. This is done using data from different models around the SU3 benchmark point and shown in figure 5.3. The relation extracted from these plots is

$$m_{IP} = (0.47 \pm 0.02)m_{EP} + (15 \pm 2)GeV\,. \tag{5.4}$$

This method is used for the $\tau\tau$ end-point but it should be kept in mind that the calibration shown was performed for SU3 data. Ideally a similar calibration should be carried out for SU1 data too.

A fit using this function is done in figure 5.4 and this produces an end-point of $m_{EP} = 67 \pm 9^{stat} \pm 5^{syst}$ with the statistical uncertainty due to the fit parameters whereas the systematic is due to the fitting procedure itself i.e. binning and fit ranges. Further systematics should be investigated but further statistics are necessary for such a study.

### 5.3.3 Finding the right jet

For the three remaining end-points the jet originating from the initial squark comes into play and it is necessary to determine which jet should be used. This is further made difficult by the high jet multiplicity of SUSY decays. The first attempt at finding the right jet is to use the $E_T$ of the jet, since the jet in the

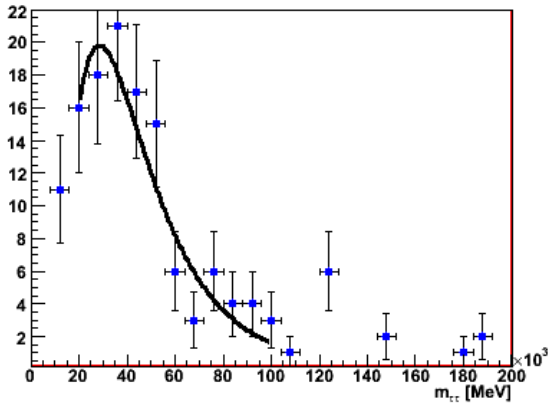


Figure 5.4: The invariant mass distribution of the OS-SS $\tau\tau$ end-point. Done using samples with CSC reconstruction.

cascade decay can be expected to have very high $E_T$. In figure 5.5 the ordering of the jet in terms of $E_T$ is plotted from generator information. As can be seen it is primarily the first (50%) and second (40%) highest $E_T$ jet that is sought.

The angular distance between the tau and the jet is plotted in figure 5.6. Shown separately are the distribution for the first and second highest $E_T$ jet and the generator level plot for comparison. In the case of the second most energetic jet there is also many jets with $\Delta R \approx 0$, which are due to taus being identified as jets. The distributions are very similar for the two and do not prove to be a good discriminant in this case.

Due to the two approaches giving similar results the highest $E_T$ jet has been chosen since that is the most likely to be the correct jet.

### 5.3.4 The $q\tau\tau$ end-point

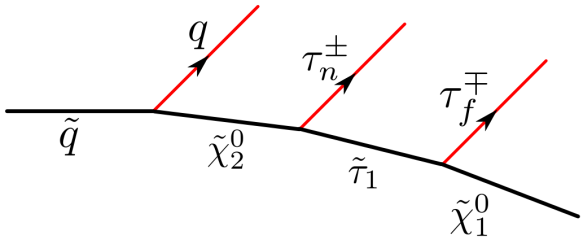


Since the end-point of the tau-tau invariant mass distribution depends on the the mass of three sparticles more end-points are necessary to determine the masses. The $q\tau\tau$ end-point provides information on the same sparticle masses as the tau-tau, in addition to the mass of the squark initiating the chain. The

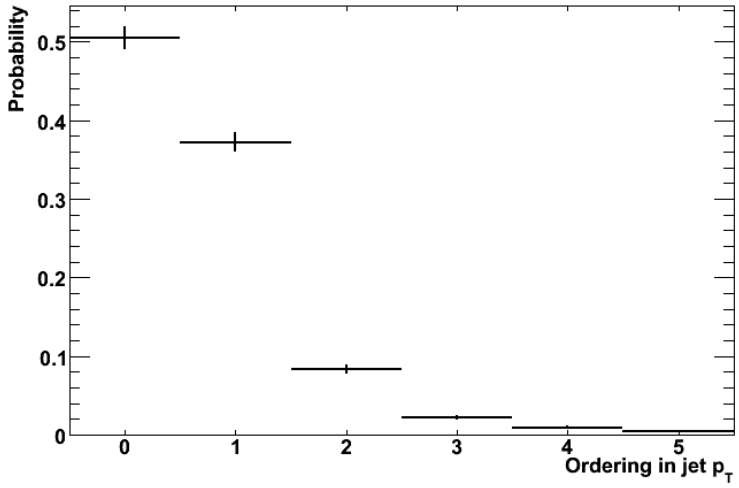


Figure 5.5: The energy ordering of the jet produced by the decay of the squark in SU1, using release 14.1.0.2 data.

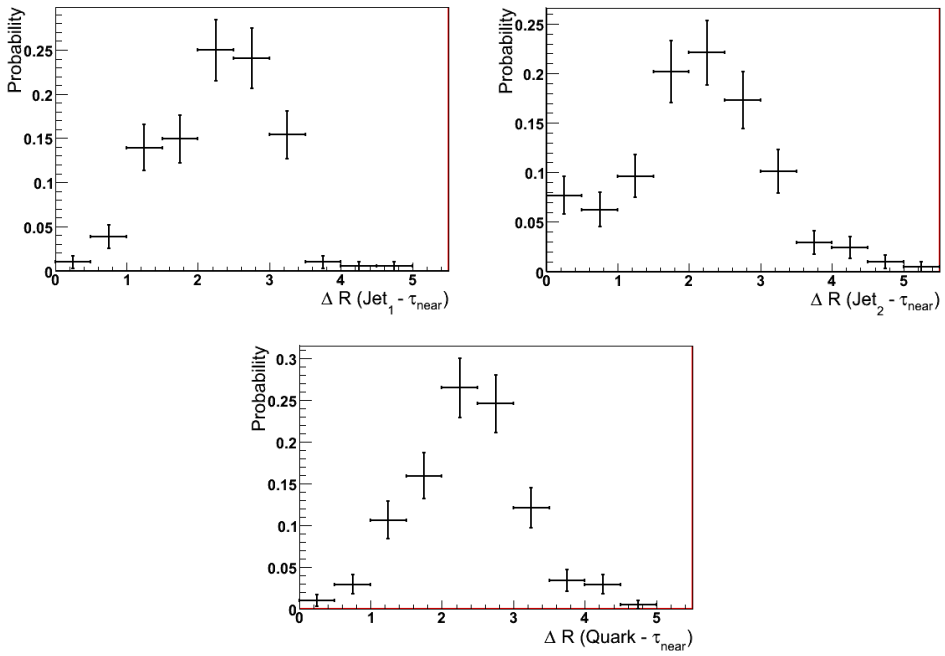


Figure 5.6: The angular distance $\Delta R$ between the jet originating from the squark and $\tau_{near}$, using release 14.1.0.2 data. In the top is reconstructed data, most energetic jet on the left and second most energetic on the right. At the bottom information from generator level is used, where the quark originating from the squark is chosen.

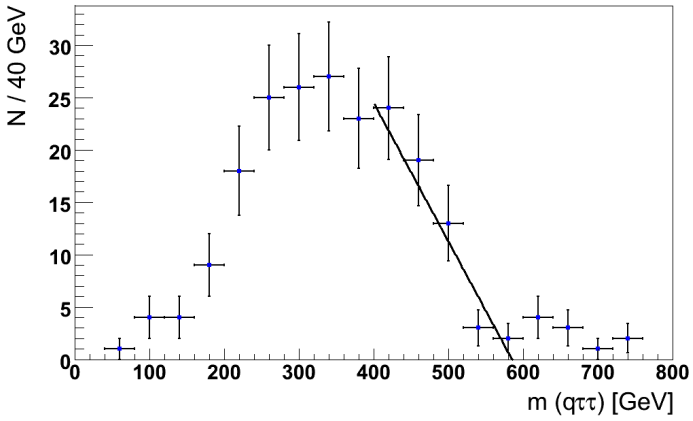


Figure 5.7: The $q\tau\tau$ invariant mass spectrum, using generator information. The distribution end-point is at $m^{max}_{q\tau\tau} = 585 \pm 10^{stat} \pm 12^{syst}$.

theoretical end-point of the distribution is at

$$m^2_{q\tau\tau} = \frac{\left(m(\tilde{q})^2 - m(\tilde{\chi}^0_2)^2\right)\left(m(\tilde{\chi}^0_2)^2 - m(\tilde{\chi}^0_1)^2\right)}{m(\chi^0_2)^2}. \tag{5.5}$$

Due to the squarks having different masses many end-points are expected to be seen here, as the distribution for each different squark initiating the chain has a separate end-point. It is neither possible to resolve the ambiguity about which squark initiated the chain in each event nor is there enough statistics to properly see each end-point unambiguously.

From truth information in figure 5.7 the end-point is found to be $m^{max}_{q\tau\tau} = 585 \pm 10^{stat} \pm 12^{syst}$, whereas the theoretical value is at 610 GeV. From the reconstructed level the values are $m^{max}_{q\tau\tau} = (586 \pm 15^{stat} \pm 18^{syst})GeV$, in agreement with the generator level fit.

### 5.3.5 The $q\tau_{far}$ and $q\tau_{near}$ end-points

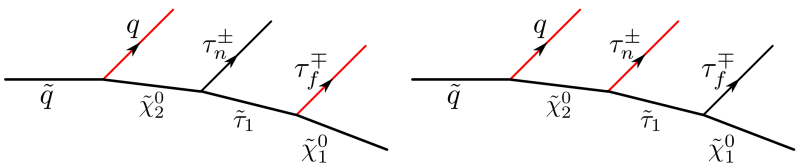


The last two end-points are formed by a combination of the jet and one of the quarks. The generator level invariant mass distributions are shown in figures 5.10 and 5.9. The theoretical values of the end-points are

$$m^2_{q\tau_{near}} = \frac{\left(m(q)^2 - m(\tilde{\chi}^0_2)^2\right)\left(m(\tilde{\tau}_1)^2 - m(\tilde{\chi}^0_1)^2\right)}{m(\tilde{\tau}_1)^2}, \tag{5.6}$$

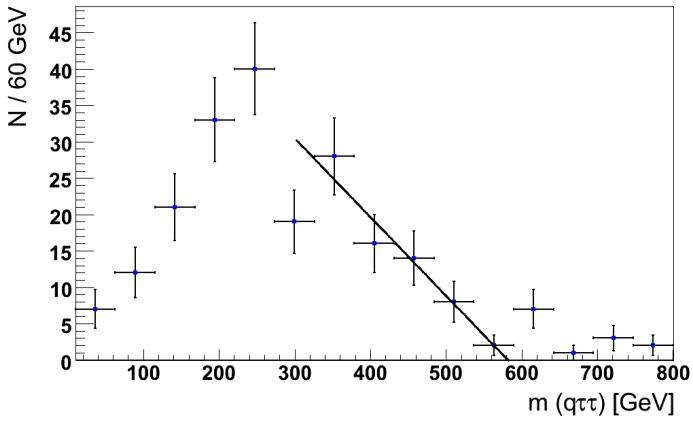


Figure 5.8: The $q\tau\tau$ invariant mass spectrum, using reconstructed data. The jet chosen is the first on in energy ordering. Reconstructed with 14.1.0.2. The fit returns an end-point at $m^{max}_{q\tau\tau} = (586 \pm 15^{stat} \pm 18^{syst})GeV$.

$$m^2_{q\tau_{far}} = \frac{\left(m(q)^2 - m(\tilde{\chi}^0_2)^2\right)\left(m(\tilde{\chi}^0_2)^2 - m(\tilde{\tau}_1)^2\right)}{m(\tilde{\chi}^0_2)^2}\,. \tag{5.7}$$

These generator level distributions are not realistic however, since it is impossible to distinguish $\tau_{near}$ from $\tau_{far}$ other than their energy difference. Therefore the low energy tau is chosen to form $q\tau_{near}$ and the high energy tau for $q\tau_{far}$. The two generator level invariant mass distributions are plotted in figures 5.11 and 5.12 where the tau is selected according to the energies of the matched taus. This requirement makes a dent in statistics since a match to reconstructed objects is needed but also gives a more realistic picture of the distributions.

The fits to the distributions on generator level produce end-points $m^{max}_{q\tau_{far}} = (336 \pm 20^{stat} \pm 18^{syst})$ GeV and $m^{max}_{q\tau_{near}} = (558 \pm 25^{stat} \pm 10^{syst})$ GeV. From reconstruction level plots, the results are similar with end-points $m^{max}_{q\tau_{far}} = (337 \pm 15^{stat} \pm 10^{syst})$ GeV and $m^{max}_{q\tau_{near}} = (558 \pm 25^{stat} \pm 10^{syst})$ GeV. As can be seen, by comparing to theoretical values in table 5.3, in both generator and reconstructed level data the $q\tau_{far}$ end-point is overestimated while the $q\tau_{near}$ is below the value expected. This is attributed to both the jet selection method and selecting the wrong tau to include in the distribution. Statistics are also quite limited making this more difficult. Furthermore, in the case of $q\tau_{near}$ the distribution is significantly different between generator and reconstruction level, this may have its origin in the jet selection as mentioned earlier but can also be due to the reconstructed jets not fully containing the entire jet.

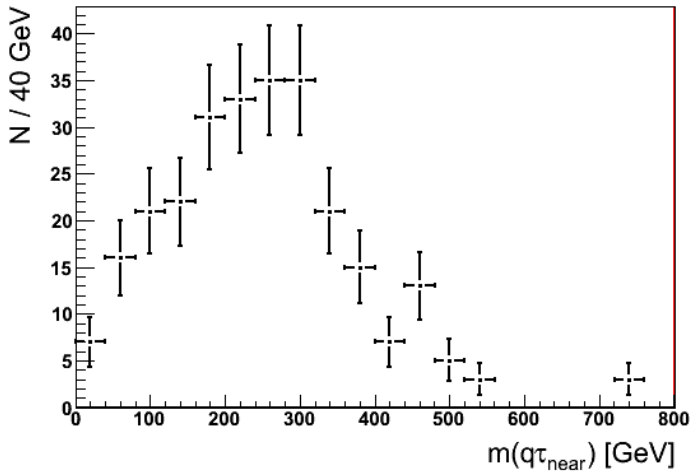


Figure 5.9: The $q\tau_{near}$ invariant mass spectrum, using generator information. The tau is required to decay from $\tilde{\chi}_2^0$.

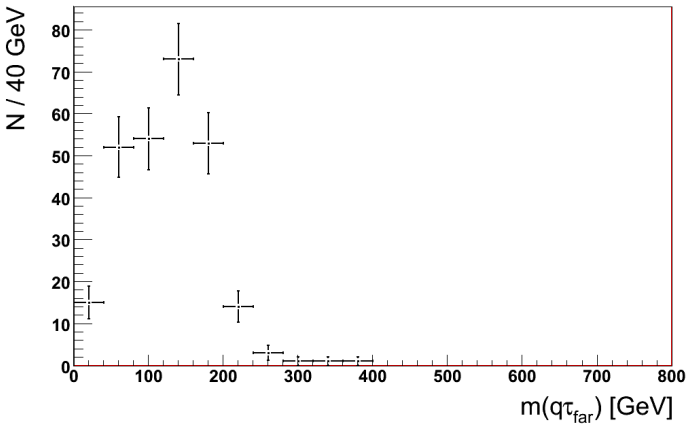


Figure 5.10: The $q\tau_{far}$ invariant mass spectrum, using generator information. The tau is required to decay from $\tilde{\tau}_1$.

Table 5.3: A summary of the end-points extracted from the data versus the theoretical predictions.

| | End-point (GeV) | | |
|---|---|---|---|
| **Distribution** | **Generator level** | **Reconstruction level** | **Theoretical** |
| $\tau\tau$ | $75.0 \pm 3.6^{stat}$ | $67 \pm 9^{stat} \pm 5^{syst}$ | 82 |
| $q\tau\tau$ | $585 \pm 10^{stat} \pm 12^{syst}$ | $586 \pm 15^{stat} \pm 18^{syst}$ | 610 |
| $q\tau_{far}$ | $336 \pm 20^{stat} \pm 18^{syst}$ | $337 \pm 15^{stat} \pm 10^{syst}$ | 270 |
| $q\tau_{near}$ | $549 \pm 14^{stat} \pm 12^{syst}$ | $558 \pm 25^{stat} \pm 20^{syst}$ | 591 |

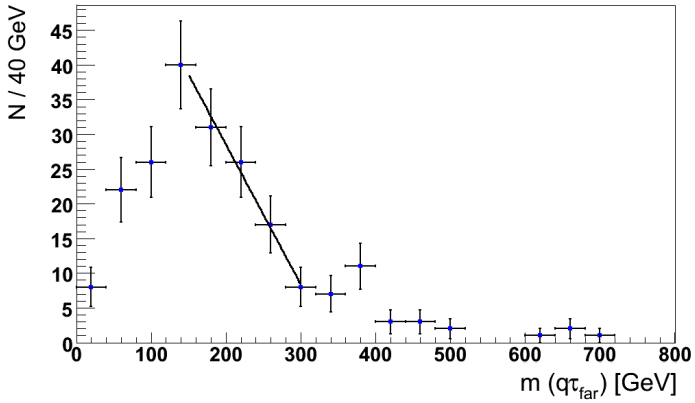


Figure 5.11: The $q\tau_{far}$ invariant mass spectrum, using generator information. The tau selected is the one with the highest reconstruction-level energy. The end-point is $m^{max}_{q\tau_{far}} = 336 \pm 20^{stat} \pm 18^{syst}$GeV.

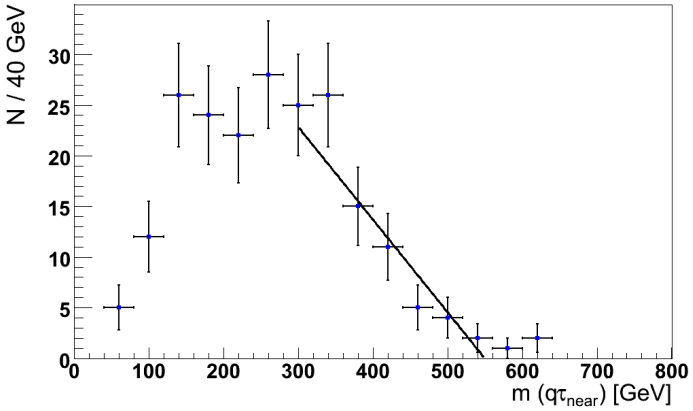


Figure 5.12: The $q\tau_{near}$ invariant mass spectrum, using generator information. The tau selected is the one with the lowest reconstruction-level energy. The end-point is $m^{max}_{q\tau_{near}} = 549 \pm 14^{stat} \pm 12^{syst}$GeV.

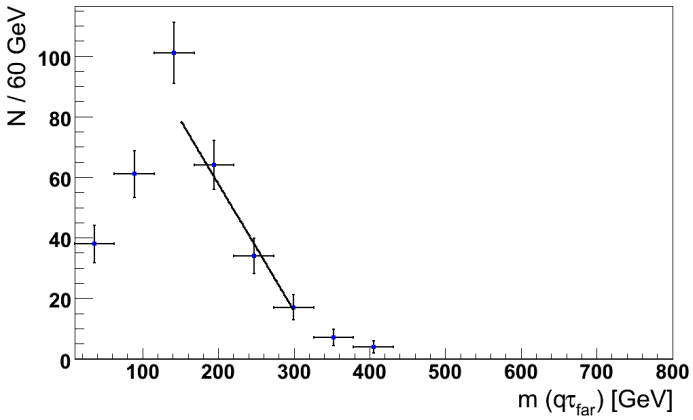


Figure 5.13: The $q\tau_{far}$ invariant mass spectrum. The end-point fit returns $m^{max}_{q\tau_{far}} = (337 \pm 15^{stat} \pm 10^{syst})$ GeV. Reconstructed with 14.1.0.2

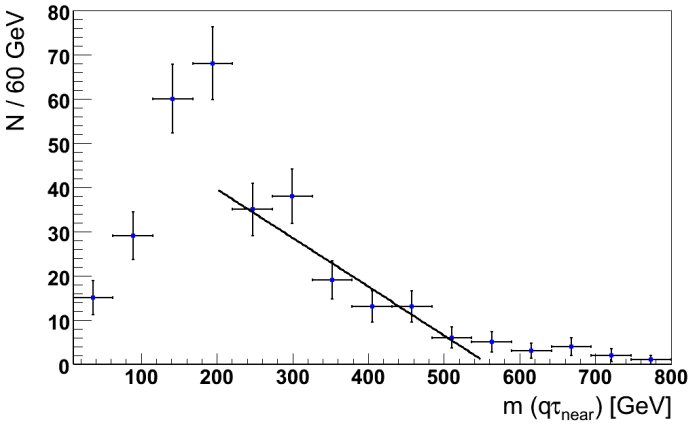


Figure 5.14: The $q\tau_{near}$ invariant mass spectrum. The end-point fit returns $m^{max}_{q\tau_{near}} = (558 \pm 25^{stat} \pm 10^{syst})$ GeV. Reconstructed with 14.1.0.2

# Chapter 6

# Summary and conclusions

In this thesis presents two main subjects were presented; the new merged tau reconstruction for ATLAS, and a determination of the end-points of invariant mass distributions of the visible decay products of decays in the SU1 mSUGRA benchmark point of ATLAS.

The new tau reconstruction algorithm, available since `Athena` release 14.0.0 was used for reconstruction. The version of `Athena` used was 14.1.0.2 and reconstruction was done privately on the CSC RDOs. Due to time and computing limitations it was only possible to reconstruct a small sample, corresponding to approximately 3 $\text{fb}^{-1}$ ( 20000 events). This is equivalent to one tenth of the CSC sample. This was only done for the signal sample however, for a full evaluation of its effect on SUSY analysis it is also necessary to look into the background samples with similar reconstuction.

The results using the new algorithm showed an improvement over the old algorithm. Tau identification was done to get similar efficiencies, the purity of the new sample was greater than in the CSC samples. Furthermore the cut placed on the $p_T$ of the leading track is lowered down to 6 GeV which is beneficial for studies such as this one, where taus can be expected to carry low energies. Further study and larger statistics are necessary to better evaluate the potential of this algorithm.

The SUSY study presented aimed to investigate four end-points of invariant mass distributions of the SU1 benchmark point which contain taus and and also to evaluate whether it is possible to determine the end-points. An overview of one of the background rejection methods that were applied is given. The method constructed can significantly reduce the background from SM processes, but higher background statistics are necessary for further optimization. This is furthermore quite necessary since the ammount of background that remains would be overwhelming.

The determination of the end-points had varying degrees of success. The determination of the tau-tau end-point was quite successful, the result being within

the statistical errors of the theoretical and generator level distribution. The remaining end-points were more problematic. The jet to be included is not easy to determine, since there are no strong angular correlations to assist in choosing the correct jet. The $q\tau\tau$ end-point is however determined without large systematic bias.

The end-points containing only one of two taus in the chain are by far the most complicated, in addition to the jet selection there is also the possibility that the wrong tau is included in them. This effect significantly alters the distributions, even when using generator level information. This makes the lower of the two end-points virtually indiscernible if the simple selection method presented is used. The larger of the two end-points was however possible to measure. The reconstructed level distribution did deviate significantly from the one done using generator information, the origin of this could either be wrong jet selection or that the reconstructed jet does not containing the entire jet.

The next step of this study would be to improve jet selection and to study dependence of the end points reconstruction on the sparticle masses involved, constructing and studying more benchmark points in the coannihilation region.

# Bibliography


[1] F. Mandl and G. Shaw, *Quantum Field Theory*, Wiley, 1993.

[2] E. Noether and M. A. Tavel, Invariant variation problems, 2005.

[3] W.-M. et al. (Particle Data Group), J. Phys. G 33, 1 (2006 and 2007 partial update for the 2008 edition).

[4] P. W. Higgs, Phys. Rev. **145**, 1156 (1966).

[5] Amaldi, Ugo and de Boer, Wim and Fürstenau, H, Phys. Lett. B **260**, 447 (1991).

[6] S. Coleman and J. Mandula, Phys. Rev. **159**, 1251 (1967).

[7] M. Tegmark et al., Physical Review D **74**, 123507 (2006).

[8] R. Haag, J. T. Lopuszánski, and M. F. Sohnius, Nucl. Phys. B **88**, 257 (1974).

[9] H. Baer and X. Tata, *Weak Scale Supersymmetry: From Superfields to Scattering Events*, Cambridge University Press, 2006.

[10] H. Baer, F. Paige, S. Protopopescu, and X. Tata, Simulating supersymmetry with isajet 7.0/ isasusy 1.0, 1993.

[11] https://twiki.cern.ch/twiki/pub/atlas/susyeventfilesinfo/isajetsu1.txt.

[12] B. K. Gjelsten, D. J. Miller, and P. Osland, JHEP **12**, 003 (2004).

[13] http://ab-div.web.cern.ch/ab-div/publications/lhc-designreport.html.

[14] The ATLAS collaboration, The ATLAS Experiment at the CERN Large Hadron Collider, Technical Report ATL-COM-PHYS-2007-102. ATL-COM-PHYS-2007-042. ATL-COM-PHYS-2007-087. ATL-COM-PHYS-2007-098, CERN, Geneva, 2007.

[15] P. Mato, GAUDI-Architecture design document, Technical Report LHCb-98-064, CERN, Geneva, 1998.

[16] T. Sjostrand, S. Mrenna, and P. Skands, JHEP **0605**, 026 (2006).

[17] G. Corcella et al., JHEP **0101**, 010 (2001).

[18] P. Bechtle et al., Identification of hadronic tau decays with ATLAS detector, Technical Report ATL-PHYS-INT-2008-003. ATL-COM-PHYS-2007-066, CERN, Geneva, 2007.

[19] W. Lampl et al., Calorimeter clustering algorithms: Description and performance, Technical Report ATL-LARG-PUB-2008-002. ATL-COM-LARG-2008-003, CERN, Geneva, 2008.

[20] E. Richter-Was, L. Janyst, and T. Szymocha, The tau1p3p algorithmimplementation in athena and performance with csc data samples, Technical Report ATL-COM-PHYS-2006-029, CERN, Geneva, 2006.

[21] M. Heldmann and D. Cavalli, An improved tau-Identification for the ATLAS experiment, Technical Report ATL-PHYS-PUB-2006-008. ATL-COM-PHYS-2006-010, CERN, Geneva, 2005.
[22] https://twiki.cern.ch/twiki/bin/view/atlas/taualgorithmmerging.
[23] https://twiki.cern.ch/twiki/bin/view/atlas/tauidentification.
[24] Oye, Ola Kristoffer and Lipniacka, Anna, ATLAS soft tau reconstruction performance in the mSUGRA stau coannihilation region, Technical Report ATL-PHYS-PUB-2006-021. ATL-COM-PHYS-2006-030, CERN, Geneva, 2006.
[25] The ATLAS collaboration, Supersymmetry searches with ATLAS at the LHC, Technical Report ATL-COM-PHYS-2008-063, CERN, Geneva, 2008, This is the SUSY chapter first submission.
[26] F. E. Paige and S. Padhi, Rome Jet Calibration Based on Athena 9.04, 2005.
[27] ATLAS Collaboration et al., Atlas detector and physics performance technical design report, Technical report, CERN-LHCC-98-13, 1999.
[28] T. Sjursen, *Search for SUSY signals with $\tau$-leptons int the ATLAS detector*, MSc thesis, Department of Physics and Technology, University of Bergen, 2008.
[29] K. Desch, T. Nattermann, P. Wienemann, and C. Zendler, Measuring the endpoint of the di-tau mass spectrum in neutralino2 decays with the atlas detector at the lhc, Technical Report ATL-PHYS-INT-2008-008. ATL-COM-PHYS-2008-038, CERN, Geneva, 2008.